













The FAST HI 21-cm absorption blind survey. II. – Statistic Exploration for Associated and Intervening Systems

WENKAI HU ^{1,2} YOUANG WANG ^{3,4,5,6} YICHAO LI ⁶ WENXIU YANG ^{3,5} YIDONG XU ^{3,4} FENGQUAN WU ^{3,4}
UE-LI PEN ^{7,8,9,10,11} JIE WANG ^{3,5} YINGJIE JING,³ CHEN XU,^{3,5} QINGZE CHEN,^{3,5} ZHENG ZHENG ^{3,12} DI LI ^{3,4,13}
MING ZHU,^{3,4,14} XIN ZHANG ^{6,15,16} AND XUELEI CHEN ^{3,4,5,6}

¹*Department of Physics and Astronomy, University of the Western Cape, Robert Sobukwe Road, Bellville, 7535, South Africa*

²*ARC Centre of Excellence for All Sky Astrophysics in 3 Dimensions (ASTRO 3D), Australia*

³*National Astronomical Observatories, Chinese Academy of Sciences, Beijing 100101, China*

⁴*Key Laboratory of Radio Astronomy and Technology, Chinese Academy of Sciences, A20 Datun Road, Chaoyang District, Beijing 100101, China*

⁵*School of Astronomy and Space Science, University of Chinese Academy of Sciences, Beijing 100049, China*

⁶*Key Laboratory of Cosmology and Astrophysics (Liaoning) & College of Sciences, Northeastern University, Shenyang 110819, China*

⁷*Institute of Astronomy and Astrophysics, Academia Sinica, Astronomy-Mathematics Building, No. 1, Sec. 4, Roosevelt Road, Taipei 10617, Taiwan, China*

⁸*Canadian Institute for Theoretical Astrophysics, University of Toronto, 60 Saint George Street, Toronto, ON M5S 3H8, Canada*

⁹*Canadian Institute for Advanced Research, 180 Dundas St West, Toronto, ON M5G 1Z8, Canada*

¹⁰*Dunlap Institute for Astronomy and Astrophysics, University of Toronto, 50 St George Street, Toronto, ON M5S 3H4, Canada*

¹¹*Perimeter Institute of Theoretical Physics, 31 Caroline Street North, Waterloo, ON N2L 2Y5, Canada*

¹²*Research Center for Intelligent Computing Platforms, Zhejiang Laboratory, Hangzhou 311100, China*

¹³*Department of Astronomy, Tsinghua University, 30 Shuangqing Road, Beijing 100084, People's Republic of China*

¹⁴*Guizhou Radio Astronomical Observatory, Guizhou University, Guiyang 550000, China*

¹⁵*National Frontiers Science Center for Industrial Intelligence and Systems Optimization, Northeastern University, Shenyang 110819, China*

¹⁶*Key Laboratory of Data Analytics and Optimization for Smart Industry (Ministry of Education), Northeastern University, Shenyang 110819, China*

ABSTRACT

We present an extragalactic HI 21-cm absorption lines catalog from a blind search at $z \leq 0.35$, using drift-scan data collected in 1325.6 hours by the ongoing Commensal Radio Astronomy FasT Survey (CRAFTS) and FAST All Sky HI Survey (FASHI), which spans a sky area of 6072.0 deg² and covers 84533 radio sources with a flux density greater than 12 mJy. 14 previously identified HI absorbers and 20 newly discovered HI absorbers were detected, comprising 15 associated systems, 10 intervening systems, and 9 systems with undetermined classifications. Through spectral stacking, the mean peak optical path, mean velocity-integrated optical path, mean FWHM and mean HI column density are measured to be 0.47 and 0.30; 27.19 and 4.36 km s⁻¹; 42.61 and 9.33 km s⁻¹; 0.49 and 0.08 T_s × 10²⁰ cm⁻² K⁻¹, for the associated and intervening samples, respectively. Statistical analysis also reveals that associated systems tend to be hosted by red ($g - r > 0.7$) galaxies at lower redshifts, whereas galaxies hosting intervening HI absorption are typically found at higher redshifts and are of a bluer ($g - r \leq 0.7$) type. A noticeable difference is observed in the positions of foregrounds, backgrounds of intervening systems, and high-redshift and low-redshift associated systems on the WISE color-color diagram. All identified foreground sources in our sample have W1-W2 magnitudes below 0.8, suggesting no Active Galactic Nuclei (AGN). In contrast, backgrounds of intervening systems tend to have W1-W2 magnitudes above 0.8, indicating AGN presence. For associated absorption, most low-redshift ($z \leq 0.5$) systems show W1-W2 values below 0.8, while higher-redshift associated absorption ($z > 0.5$) displays a broader range of W1-W2 values.

Keywords: radio lines: galaxies – radio continuum: galaxies – line: identification – line: profiles

1. INTRODUCTION

The HI 21-cm absorption lines are spectral features that arise from foreground gas absorbing the flux of a background bright radio source. Since the detectability of HI absorption depends only on the column density of foreground gas and the strength of background radio sources, it could be a complement to the observation of HI emission at higher redshifts, where direct detection of emission becomes challenging. HI absorption is an excellent tool to measure HI content and constrain redshift-evolution of cosmic HI relative density (Ω_{HI}) at intermediate redshifts $0.2 < z < 2$, probe physical conditions in ISM (Heiles & Troland 2003; Wolfire et al. 2003; Morganti & Oosterloo 2018), trace mergers and interactions of galaxies (Dutta et al. 2018; Varenus et al. 2017), reveal evolution history of SFR density (Curran 2017; Dutta 2019), place stringent constraints on variation of fundamental constants of physics (Rahmani et al. 2012) and provide direct proof of cosmic acceleration (Darling 2012; Yu et al. 2014; Kloeckner et al. 2015; Jiao et al. 2020; Lu et al. 2023).

In the study of HI absorption systems, there are two primary categories. The first is the (source) associated absorption system, where the gas absorbing the light is located in the same extragalactic object (often an AGN) that emits the bright continuum. Research in this area primarily focuses on the AGN itself and its interaction with Interstellar Medium (ISM) in the same extragalactic object. This research includes examining the kinematics and structure of the ISM in galaxies hosting AGNs and exploring how HI gas might fuel supermassive black holes (SMBH)(see (Morganti & Oosterloo 2018) and the references therein).

The second category is known as the intervening absorption system, which occurs when gas in a foreground galactic or extragalactic object absorbs light from a bright, unrelated background source. These systems are commonly used to study ISM properties of both Galaxy (Dickey et al. 2013, 2022) and distant galaxies (Sadler et al. 2020). A significant portion of post-reionization universe’s neutral hydrogen is found in the Damped Lyman-alpha systems (DLAs, $N_{\text{HI}} \geq 2 \times 10^{20} \text{ cm}^{-2}$; (Wolfe et al. 2005)), observed in absorption lines of optical quasi-stellar objects (QSOs). However, the bright light from the background QSOs blinds the direct study of DLAs themselves. Despite extensive research, the precise physical nature of DLAs remains an unresolved issue (for recent work, see, e.g. Bordoloi et al. 2022). Although associated HI absorption can reach DLA-level

column densities, it is considered separately due to its proximity to host galaxies, unlike intervening DLAs along random sightlines. DLAs typically refer to intervening systems that reveal the large-scale distribution of neutral hydrogen across cosmic time.

Despite significant advances in this field, current findings are constrained by limited sample sizes and biases resulting from previously chosen targets. Conducting an unbiased large radio survey would directly tackle the DLA issue, helping to surmount these restrictions. Additionally, it would offer a more thorough understanding of the interaction between the AGN and the ISM of the host galaxy.

Due to the limitation that only HI gas along the line of sight to the background radio source can be traced, and considering the sensitivity of the telescopes, only a small number of HI absorption systems have been detected through blind surveys. Recently, there have been promising developments in the search for HI absorption systems, utilizing the capabilities of advanced radio telescopes from the latest generation, including Allison et al. (2020); Su et al. (2022); Aditya et al. (2024) from the First Large Absorption Survey in HI (FLASH; Allison et al. 2022), Gupta et al. (2021); Deka et al. (2024a) from the MeerKAT Absorption Line Survey (MALS; Deka et al. 2024b), and the searches described below with FAST.

As the largest single-dish telescope in the world, FAST (Nan et al. 2011; Jiang et al. 2020) is equipped with a multibeam feed system and low-noise cryogenic receivers, ideal for conducting large blind HI absorption surveys. Research efforts using HI absorption have been successfully conducted by FAST, including studies on cosmic acceleration (Kang et al. 2024), constraining the OH-to-HI relative abundance ($[\text{OH}]/[\text{HI}]$) (Zheng et al. 2020), and both targeted (Zhang et al. 2021; Chandola et al. 2024; Yu et al. 2023) and blind Zhang et al. (2021); Hu et al. (2023) HI absorption searches. These studies highlight that FAST is an excellent telescope for conducting HI absorption science.

In Hu et al. (2023, hereafter Paper I), we carried out a purely blind HI absorption survey in the 1300-1450 MHz band of 3155 deg^2 CRAFTS data. Three known associated absorbers (UGC 00613, 3C 293 and 4C +27.14) and two new absorbers (NVSS J231240-052547 and NVSS J053118+315412) were detected. The search technique detailed in Paper I was then extended to a broader range of CRAFTS (Li et al. 2018) and FASHI (Zhang et al.

2024) data, leading to a discovery of an increased number of HI 21cm absorption features.

In this paper, we report a 21cm-selected sample of HI absorption from a purely blind search in the 1050–1450 MHz band in the sky covered by the CRAFTS and FASHI (1325.6 hours and 6072.0 deg²). Another 11 known HI absorbers and 18 new HI absorbers are found using our search pipeline. Combined with Paper I, a sample of 34 21cm-selected HI absorption systems is obtained. We made a comprehensive statistical study for the intervening and associated absorption.

This paper is organized as follows: Section 2 describes the survey data and follow-up observation used in this work. We summarize data processing, candidate selection method and HI absorption measuring method in Section 3. The physical properties of confirmed HI absorption are presented in Section 4. Section 5 statistically studies the characters of associated and intervening absorption systems. We discuss the comoving absorption path and statistic completeness in Section 6. In Section 7 a summary of this work is presented. Throughout this paper we use $H_0 = 70 \text{ km s}^{-1} \text{ Mpc}^{-1}$, $\Omega_m = 0.3$ and $\Omega_\Lambda = 0.7$.

2. DATA

2.1. Radio Data

2.1.1. CRAFTS

CRAFTS is a multi-purpose drift-scan survey that aims to observe galactic and extragalactic HI emissions, measure continuum signals, and search for new pulsars and fast radio bursts (FRB). The survey uses the FAST L-band Array of 19 feed-horns (FLAN, Dunning et al. (2017)) covering the frequency band from 1050 MHz to 1450 MHz. CRAFTS drift scans started in early 2020 with the 19-beam feed rotated by 23.4° to achieve a super-Nyquist sampling while drifting. Two-pass drift scans are planned to be made and over 22000 deg² within a declination (Dec) range between -14° and 66° . Limited by allocated time, there is only one survey pass at present.

2.1.2. FASHI

FASHI is a comprehensive observational initiative designed to map the sky accessible by FAST, encompassing an area of about 22,000 square degrees within declinations from -14° to 66° and frequencies between 1050 and 1450 MHz. The primary objective of FASHI is to conduct a detailed survey of HI gas in the nearby universe, with an additional goal to catalog at least 100,000 HI galaxies. The survey employed a strategy of fixing declination and conducting drift scans throughout the project. From August 2020 to June 2023, FASHI

successfully surveyed over 7,600 square degrees, achieving a median sensitivity of approximately 0.76 mJy beam⁻¹ and a spectral line velocity resolution of about 6.4 km s⁻¹ at 1.4 GHz. In their findings, Zhang et al. (2024) reported the detection of 41,741 extragalactic HI sources within the frequency range of 1305.5–1419.5 MHz, which corresponds to a redshift limit of $z \leq 0.09$.

As of August 29, 2023, our search has been conducted in part of the CRAFTS and FASHI regions, marked by the orange and green labels in Figure 1.¹

2.1.3. Follow-up Observation

In the blind searching in CRAFTS data, a total of 34 candidates, including 14 previously known HI absorption systems and 20 newly discovered ones are detected. All absorption systems are verified by the CRAFTS data of several neighboring beams with a high signal-to-noise ratio. To confirm the signal of these 20 first discovered candidates and obtain a more significant HI absorption feature for known absorption systems, we made several follow-up observations with FAST from 2021 to 2023.

To suppress the fluctuations in bandpass and remove the sky signal, follow-up observations used ON-OFF tracking mode. The integration time for both the source-on and source-off observations is set as 990s. A cycle of 330s source-on followed by 330s source-off observation is repeated 3 times for each target. The data set of follow-up observations has a time resolution of 1 s, and a frequency resolution of 7.63 kHz (equivalent to 1.6 km s⁻¹ at the redshift of 0), covering the frequency from 1050 MHz to 1450 MHz. A noise level of 0.338 mJy/beam can be achieved with an integration time of 990 seconds and a frequency resolution of 7.63 kHz.

2.2. Infrared Data

We extract the infrared properties of the absorption systems from the Wide-field Infrared Survey Explorer (WISE; Wright et al. 2010) data. WISE is an all-sky survey mapping the infrared sky at 3.4, 4.6, 12, and 22 μm (W1, W2, W3, and W4) with angular resolutions of 6.1 arcsec, 6.4 arcsec, 6.5 arcsec and 12.0 arcsec in the four bands respectively. We recognize the WISE counterparts of the HI absorption systems using the NASA/IPAC Extragalactic Database (NED, Helou et al. 1991). WISE continuum map, if available, for each HI absorption system is extracted from the NASA/IPAC Infrared Science Archive (IRSA) and presented below.

¹ Further information about the finished scans can be found in <http://groups.bao.ac.cn/ism/CRAFTS/CRAFTS/>.

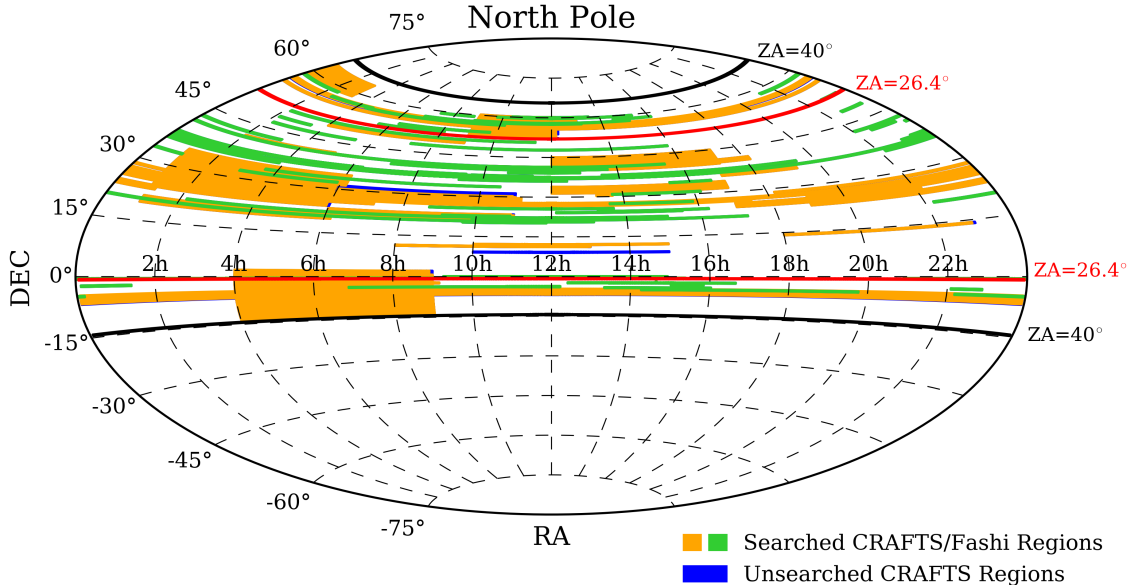


Figure 1. Up-to-date (2023-08-29) CRAFTS sky coverage in Equatorial coordinates. Search areas in CRAFTS and FASHI regions are highlighted by orange and green labels, respectively. Blue regions refer to CRAFTS sky that has not been searched. Zenith angle of 40° (maximum zenith angle for FAST) and 26.4° (zenith angle within which FAST has full gain) are shown as black circles and red circles, respectively.

The $W1-W2 > 0.8$ (Stern et al. 2012) threshold is a widely used and reliable diagnostic for identifying AGN in mid-infrared surveys like WISE. AGNs exhibit a characteristic infrared excess caused by hot dust near the central black hole (Fritz et al. 2006), which emits strongly in the W2 band, leading to a $W1-W2$ color greater than 0.8. In this work, we use the $W1-W2$ threshold to infer the origin of the infrared emission and assess the presence of AGN associated with each HI absorption. Additionally, the WISE color-color diagram (Wright et al. 2010) is a valuable tool for identifying and classifying various types of astronomical objects based on their infrared properties. This method is employed in our analysis to classify object types (see Section 5.2).

2.3. Optical Data

The optical observation data of our background sources are obtained from the Sloan Digital Sky Survey (SDSS, York et al. 2000) Data Release 16. The optical counterparts of the background/foreground sources are selected by cross-matching the coordinates of the sources with the SDSS catalog using a 2-arcsec matching radius. Among the 29 HI absorption detections presented in this paper, 6 are outside the footprint of SDSS.

3. ANALYSIS

3.1. Searching Algorithms

Considering both CRAFTS and FASHI surveys have been conducted in the drift-scan mode, we rebinned the

data into a time resolution of $\sim 12/\cos\delta_{\text{dec}}$ s (\sim the transit time in drift scan, where δ_{dec} is the declination of the pointing) and a frequency resolution of $\Delta\nu = 15.26$ kHz, and applied the same data-processing method to them. The search technique has been described in detail in Paper I. In summary, after the removal of the baseline (estimated using a low-pass filter), HI absorbers are blindly searched by cross-correlating flux spectra with Gaussian templates (matched-filtering approach, (Saintonge 2007)). We searched for HI absorption signal in both XX and YY polarizations of each beam. We select candidates with a combined velocity-integrated signal-to-noise ratio (S/N) exceeding 5.5 and those that are found at nearly the same frequency ($\delta f < 0.04$ MHz) with an individual S/N exceeding 3.5 in both XX and YY polarizations. Final candidates are selected by use of transit information recorded by the 19-beams of FAST.

3.2. HI Absorption Measurement

HI 21-cm absorption lines arise from foreground HI gas absorbing the flux of the background bright radio source. The HI column density of the foreground gas can be calculated by integrating observed absorption over velocity (Morganti & Oosterloo 2018):

$$N_{\text{HI}} [\text{cm}^{-2}] = 1.82 \times 10^{18} T_s [\text{K}] \int \tau(V) dV [\text{km s}^{-1}], (1)$$

where $\tau(V)$ and T_s refer to optical depth and spin temperature of the HI source, respectively. Under the as-

sumption that $T_s \ll c_f T_c$, the optical depth $\tau(V)$ can be expressed as:

$$\tau(V) = -\ln(1 + \Delta T(V)/(c_f T_c)), \quad (2)$$

where c_f is covering factor. T_c is the brightness temperature of the background continuum source, which was deduced from the line-free parts of the spectrum in this work. $\Delta T(V)$ is the difference between the observed signal of HI gas and brightness temperature of background continuum source. If $T_s > c_f T_c$, the spectral line will be seen in emission, while if $T_s < c_f T_c$, absorption dominates.

Throughout this paper we take the assumption that $T_s \ll c_f T_c$ and $c_f = 1$ (Maccagni et al. 2017) for the calculation of τ and N_{HI} . The new HI absorption will be classified as ‘‘associated absorption’’ if the velocity difference between the HI absorption and the background is within 1500 km s^{-1} .

4. VERIFIED HI ABSORPTION SYSTEMS

From August 2021 to October 2023, we conducted follow-up observations using FAST in the ON-OFF tracking observation mode, with 990 seconds of on-source integration for each absorption system. In total, we verified 34 HI absorption, comprising 14 previously known absorbers and 20 newly discovered ones. The spectra of these HI absorption were calibrated using a built-in noise diode that was activated for 1 second every 8 seconds. To remove the bandpass baseline, a polynomial function was fitted to the absorption line-free parts of the spectrum. A Doppler shift correction was then applied to each absorption spectrum. Finally, we employed multi-component Gaussian functions to fit the profiles of authentic HI absorption.

For each source, we display the absorption spectrum along with its Gaussian fitting. Additionally, we present an image centered on the radio source, created by using radio data at S-band from the Karl G. Jansky Very Large Array Sky Survey (VLASS, Lacy et al. (2020)), along with infrared data from WISE and optical data from SDSS (when available).

We document the fundamental physical information for each radio source in Table 1. Tables 2 and 3 display infrared and optical magnitudes corresponding to the WISE and SDSS counterparts of the radio sources, respectively. Table 4 shows the measurements of HI absorption signals and the corresponding HI column densities for previously identified absorption. Additionally, Table 5 provides the same information for the newly detected absorbers.

4.1. Previously Known Absorbers

4.1.1. 4C +56.02

4C+56.02 is also a little-studied bright compact radio source. The absence of redshift data for 4C+56.02 has left the identification of the foreground counterpart in an uncertain state, emphasizing the need for further high-resolution follow-up observations to attain clarity. Dickey & Benson (1982) used the 91m- and 43m- single-dish telescopes as an interferometer to observe its 21-cm line, and reported the parameter of absorption as peak optical depth $\tau_{\text{peak}} \sim 0.48$ and $N_{\text{HI}} \sim 22.44 \times 10^{20} \text{ cm}^{-2} \text{ K}^{-1}$.

We blindly re-detected its absorbing profile and presented its absorption spectrum in the left panel of Figure 2. Its absorption spectrum is well-fitted using the six-components Gaussian function. Our measurements of the HI absorption towards 4C+56.02 give a flux density depth of $S_{\text{HI,peak}} \sim -885.85 \text{ mJy}$ and FWHM of $\sim 46.32 \text{ km s}^{-1}$, peak optical depth $\tau_{\text{peak}} \sim 0.55$ and $N_{\text{HI}} \sim 0.47 T_s \times 10^{20} \text{ cm}^{-2} \text{ K}^{-1}$.

4.1.2. 4C +31.04

4C+31.04 (Figure 3) is a GHz-peaked spectrum (GPS) and Compact Steep Spectrum (CSS) source with compact-symmetric-object (CSO) morphology (Giroletti et al. 2003; Ostorero et al. 2017). The host galaxy of 4C+31.04 is MCG 5-4-18, a giant elliptical galaxy with a Seyfert 2-like optical spectrum. 4C+31.04 has two asymmetric lobes, suggesting strong interactions between the jets and a dense ISM (Giovannini et al. 2001). Shocked molecular and ionized gas resulting from jet-driven feedback in 4C+31.04 was observed and reported by Zovaro et al. (2019). The jet-blown bubble pushes a forward shock into ambient ISM, giving rise to [Fe II] emission. The H_2 emission, arising from the shock-excited molecular gas, is also detected. 4C+31.04 has a close companion, MCG 5-4-17, which is a spiral galaxy at a projected distance of $\sim 20 \text{ kpc}$ and a velocity offset of 1560 km s^{-1} .

The WISE counterpart to 4C+31.04 given by NED is WISEA J011935.00+321050.2. WISEA J011935.00+321050.2 has a W1-W2 of 0.021, indicating that the mid-IR emission comes mainly from stars.

The HI absorption associated with 4C+31.04 was firstly reported in van Gorkom et al. (1989) with a velocity of $17391 \pm 3 \text{ km s}^{-1}$, a FWHM of $153 \pm 6 \text{ km s}^{-1}$, peak optical depth $\tau_{\text{peak}} \sim 0.037$ and $N_{\text{HI}} \sim 0.096 T_s 10^{20} \text{ cm}^{-2} \text{ K}^{-1}$. Gupta et al. (2006) presented the results of HI and OH absorption measurements towards 4C+31.04 using the Arecibo 305-m telescope, giving the peak optical depth $\tau_{\text{peak}} \sim 0.038$ and $N_{\text{HI}} \sim 0.122 T_s 10^{20} \text{ cm}^{-2} \text{ K}^{-1}$. Struve & Conway (2012) presented Very Long Baseline Array (VLBA) HI absorp-

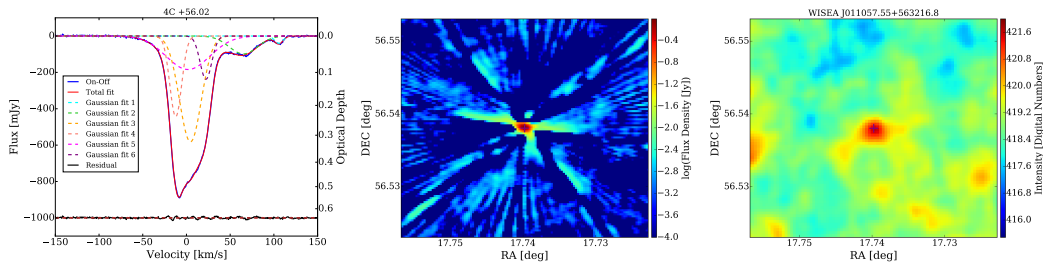


Figure 2. Left: HI absorption feature of 4C +56.02. The blue solid line shows the absorption spectrum and the red solid line shows the fit with a six-component Gaussian model. The fitting residual is shown as a black-solid line at the bottom. The optical depth value for HI absorption is shown on the right scale. Middle: the radio map from VLASS centered at 4C +56.02. Right: the W3 band infrared map centred at 4C +56.02.

tion observations of the circumnuclear environments of 4C +31.04, and absorption was detected against the core and both lobes.

We blindly re-detected its associated absorbing profile and updated its parameter by use of the data from the follow-up observation. We present the up-to-date finest structure of its absorption profile in Figure 3, which is fitted by the seven-components Gaussian function. Our measurements of the HI absorption associated with 4C +31.04 give a flux density depth of $S_{\text{HI, peak}} \sim -108.96$ mJy, an FWHM of ~ 151.94 km s $^{-1}$, $\int \tau dv \sim 6.55$ km s $^{-1}$ and $N_{\text{HI}} \sim 0.119T_s 10^{20}$ cm $^{-2}$ K $^{-1}$, which is consistent with van Gorkom et al. (1989) and Gupta et al. (2006).

Besides the broad absorption centered at 17926.39 km s $^{-1}$, a narrow absorption component at 18152.40 km s $^{-1}$ is also detected in the CRAFTS data. Our detection of the sub-absorption is consistent with the absorption profile presented in van Gorkom et al. (1989) and Struve & Conway (2012). 4C +31.04 does not show any sign of recent interaction such as tidal tails (Perlman et al. 2001). On the other hand, the velocity offset between 4C +31.04 and its companion far exceeds the measured velocity difference between broad and narrow absorption (~ 200 km s $^{-1}$). The narrow absorption may come from another un-discovered optical-faint but gas-rich companion galaxy (Struve & Conway 2012).

4.1.3. 3C 84 (NGC 1275)

NGC 1275 (Figure 4) is a giant cD elliptical galaxy situated close to the center of the Perseus cluster, stands out as the nearest cool-core cluster Brightest Cluster Galaxy (BCG) detected with HI, showcasing a rich cluster environment (Saraf et al. 2023). The galaxy hosts an active nucleus, evident through the presence of the powerful compact radio source 3C 84. Positioned in front of NGC 1275 is another high-velocity system (HVS) at around 8200 km s $^{-1}$, observable in both H α emission (Caulet et al. 1992) and HI absorption (De Young et al. 1973). Through comprehensive global VLBI observa-

tions, Momjian et al. (2002) presented a high dynamic range image of this HI absorption feature, detecting six distinct absorption peaks that suggest the presence of multiple HI clouds. The likely nature of the foreground object is a gas-rich galaxy.

In addition to the HI absorption associated with the HVS, a broad HI absorption feature centered on the systemic velocity of NGC 1275 (around 5300 km s $^{-1}$) was also detected (Jaffe 1990). Recently, Morganti et al. (2023), using JVLA and VLBA observations, detected both narrow and broad HI absorptions with arcsecond resolution. By comparing the properties of the HI absorption to those of the molecular circumnuclear disc (CND) in NGC 1275, they concluded that the HI arises from the fast-rotating CND, and that neutral atomic hydrogen is present as close as 20 pc from the SMBH. Additionally, with the JVLA, they discovered a new, faint absorbing system redshifted by approximately 2660 km s $^{-1}$ relative to NGC 1275, which they identified as gas stripped from a foreground galaxy falling into the Perseus cluster.

In our data, we re-detected the previously known narrow and broad HI absorptions associated with the HVS and NGC 1275. As shown in Figure 4, our measurements are in close agreement with those from earlier studies.

4.1.4. 4C -06.18

4C-06.18 (Figure 5) is a little-studied bright radio source, its redshift information is unavailable, leaving the counterpart to the foreground in an uncertain state. It necessitates additional high-resolution follow-up observations. The absorption towards 4C-06.18 was firstly and exclusively reported by Roger et al. (1978), with the following absorption parameters: peak optical depth $\tau_{\text{peak}} \sim 1.4$, $\int \tau dv \sim 4.5$ km s $^{-1}$ and $N_{\text{HI}} \sim 2.9 \times 10^{20}$ cm $^{-2}$ (spin temperature $T_s \sim 35$ K), which are close to our measurements. We blindly re-detected its absorbing profile and obtained its fine structure in the follow-up observation. Its absorption spectrum is well-fitted using the six-components Gaussian function and

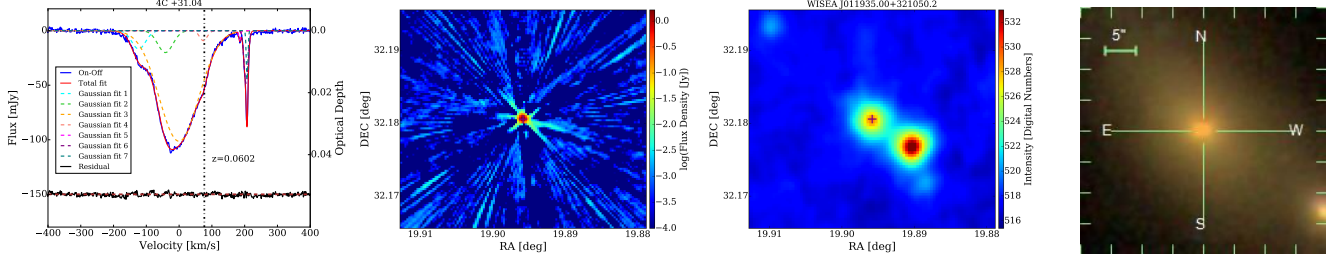


Figure 3. Left: same as Figure 2, but for 4C+31.04. The black dot-dashed vertical line marks the redshift as given in the NED. Middle left: radio map from VLASS centered at 4C+31.04. Middle right: W3 band infrared map of WISEA J011935.00+321050.2 from WISE. Right: optical map of 4C+31.04 from SDSS.

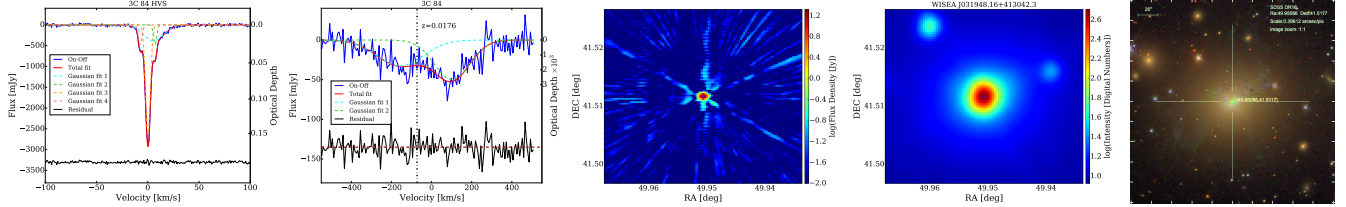


Figure 4. Left and Middle Left: same as Figure 2, but for 3C 84 HVS and 3C 84. Middle: the radio map from VLASS centered at 3C 84. Middle right: W2 band infrared map of WISEA J031948.16+413042.3 from WISE. Right: SDSS optical map of the optical counterpart of WISEA J031948.16+413042.3.

is shown in the left panel of Figure 5. The strongest HI absorption profile exhibits a nearly symmetric and narrow profile, likely originating from a gas disk. Additionally, there is a broader wing with two shallower peaks at lower redshifts, indicating the existence of unsettled gas structures and a potential jet of gas.

4.1.5. NVSS J085521+575143

Intervening absorption is found towards NVSS J085521+575143, the background source is identified as an FR II radio source (Biggs et al. 2016) and a CSO with two lobes separated by approximately 55 mas (Helmboldt et al. 2007) (Figure 6). The distorted appearance of the background radio source suggests a strong jet–cloud interaction in its host galaxy (Biggs et al. 2016). The absorption towards NVSS J085521+575143 was initially reported by Zwaan et al. (2015), the absorption parameters were reported as peak optical depth $\tau_{\text{peak}} \sim 0.24$ and $\int \tau dv \sim 1.02$, which closely aligns with our findings.

The SDSS counterpart to the foreground galaxy is SDSS J085519.05+575140.7, whose magnitudes are $u=19.437$, $g=17.765$, $r=17.265$, $i=17.043$ and $z=16.834$. The WISE counterpart to SDSS J085519.05+575140.7 given by NED is WISEA J085519.02+575140.7. The WISE W1[3.4 μm], W2[4.6 μm], W3[12.1 μm] and W4[22.2 μm] magnitudes for WISEA J085519.02+575140.7 are 15.535 ± 0.047 , 15.288 ± 0.105 , 11.935 ± 0.214 and 8.706 , respectively. The W1-W2 color of WISEA J085519.02+575140.7 is 0.247, which indicates that the mid-IR emission comes mainly

from stars. According to the W2-W3 value of 3.353 mag, WISEA J085519.02+575140.7 is located in the intersection of the Spirals region and the LIRGs region in the WISE color–color diagram.

4.1.6. NVSS J112832+583346 (NGC 3690)

NGC 3690 (Figure 7) is within the nearby ($cz = 3121 \text{ km s}^{-1}$) merging system recognized as Arp 299 or Mrk 171. Positioned in the early stages of a merger, this system comprises NGC 3690, constituting the western portion of the merger, and IC 694, serving as the eastern component. The exceptional burst of star formation in Arp 299 is evidenced by strong 10 μm emission (Gehrz et al. 1983), extended H_2 features (Fischer et al. 1983), and optical emission fluxes (Weedman 1972; Augarde & Lequeux 1985). The total molecular gas mass (M_{H_2}) derived for Arp 299 is $6 \times 10^9 M_{\odot}$, with M_{HI} exceeding $6 \times 10^9 M_{\odot}$ (Casoli et al. 1989). The system exhibits a high infrared luminosity, $L_{\text{IR}} = 5 \times 10^{11} L_{\odot}$, attributed to re-radiation of dust heated by remarkable starburst activity, with no discernible evidence of an AGN within the system.

The detection of HI absorption linked to NGC 3690 was initially documented by Dickey & Benson (1982); Dickey (1986). Subsequently, employing the VLA, Baan & Haschick (1990) identified HI absorption across all locations within Arp 299, revealing sixteen distinct velocity components. The HI gas originating from IC 694 is observed in absorption at the nucleus of NGC 3690, and vice versa.

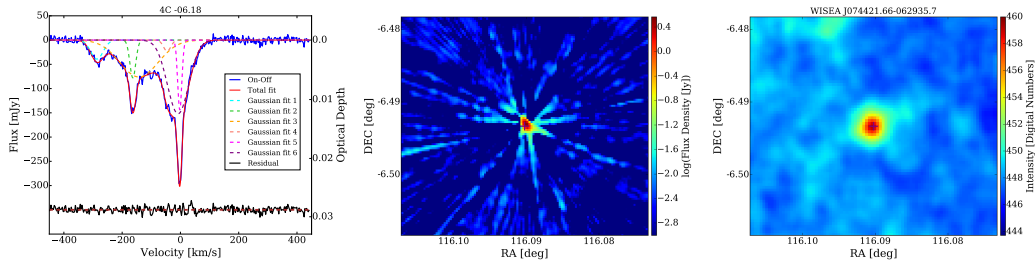


Figure 5. Left: same as Figure 2, but for 4C-06.18. Middle: the radio map from VLASS centered at 4C-06.18. Right: the W3 band infrared map from WISE centered at 4C-06.18.

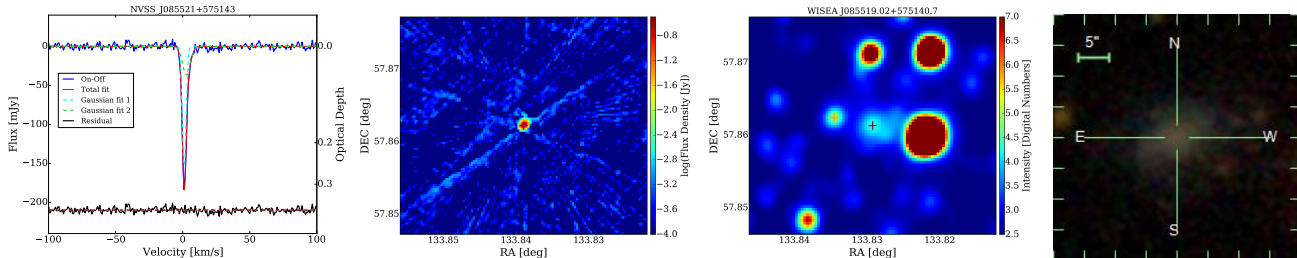


Figure 6. Left: same as Figure 2, but for NVSS J085521+575143. Middle left: radio map from VLASS centered at NVSS J085521+575143. Middle right: W1 band infrared map of WISEA J085519.02+575140.7 (shown as a purple cross) and WISEA J085519.81+575141.1 (WISE counterpart to background NVSS J085521+575143, shown as an orange cross) from WISE. Right: SDSS optical map of the optical counterpart of WISEA J085519.02+575140.7.

We blindly detected HI absorption in Arp 299 in the FAST survey. The FAST beam, with a size of 3 arcmins, covers the entire merging system and captures emissions and absorption in front of the extended continuum sources (depicted in Figure 7). Our spectra align with those of Casoli et al. (1989), who presented HI spectra obtained using the Nançay telescope (with a beam size of 4 arcminutes \times 20 arcminutes).

In our observed absorption profile, two components are discernible. Given that NGC 3690 is nearly face-on and IC 694 is almost edge-on, it is reasonable to infer that the velocity component around 3184 km s^{-1} corresponds to gas from IC 694, while the component at 3094 km s^{-1} belongs to NGC 3690 (Baan & Haschick 1990). However, due to the limitations of our single-dish observation, which can not differentiate HI absorption in each object within Arp 299, we cannot provide accurate estimates for optical depth and column density.

4.1.7. NVSS J134035+444817

NVSS J134035+444817 (Figure 8) is categorized as a Flat-Spectrum Radio Source in Healey et al. (2007). Within the CORALZ sample, this radio source is identified as a potential compact core-jet (CJ) source (de Vries et al. 2009). The linked HI absorption was initially documented by Geréb et al. (2015). A slender HI absorption profile is observed at the velocity of NVSS J134035+444817, suggesting the presence of a gas disk.

4.1.8. 4C +57.23

The HI absorption observed toward 4C +57.23 (Figure 9) is identified as intervening absorption. The SDSS counterpart linked to the foreground galaxy is SDSS J135400.68+565000.3. Its magnitudes are $u=19.783$, $g=17.964$, $r=16.976$, $i=16.546$ and $z=16.200$. Based on the SDSS image, this galaxy appears to be an edge-on spiral galaxy, likely of morphological type Sa. The presence of HI absorption in SDSS J135400.68+565000.3 toward 4C+57.23 was initially documented by Zwaan et al. (2015). In our blind detection, we reconfirmed this absorption and obtained measurements closely aligned with Zwaan et al. (2015), who reported a peak optical depth of $\tau_{\text{peak}} \sim 0.14$ and $\int \tau dv = 3.03 \text{ km s}^{-1}$.

The WISE counterpart to the foreground SDSS J135400.68+565000.3 is WISEA J135400.67+565000.5 according to NED. WISE W1[3.4 μm], W2[4.6 μm], W3[12.1 μm] and W4[22.2 μm] magnitudes for WISEA J135400.67+565000.5 are 13.901 ± 0.026 , 13.803 ± 0.035 , 12.464 ± 0.278 and 9.192 , respectively. W1-W2 color of WISEA J135400.67+565000.5 is 0.098, which suggests that the mid-IR emission comes mainly from stars. According to the W2-W3 value of 1.339 mag, WISEA J135400.67+565000.5 is located in the intersection of the Spirals region and the Ellipticals region in the WISE color-color diagram.

4.1.9. NVSS J141314-031227 (NGC 5506)

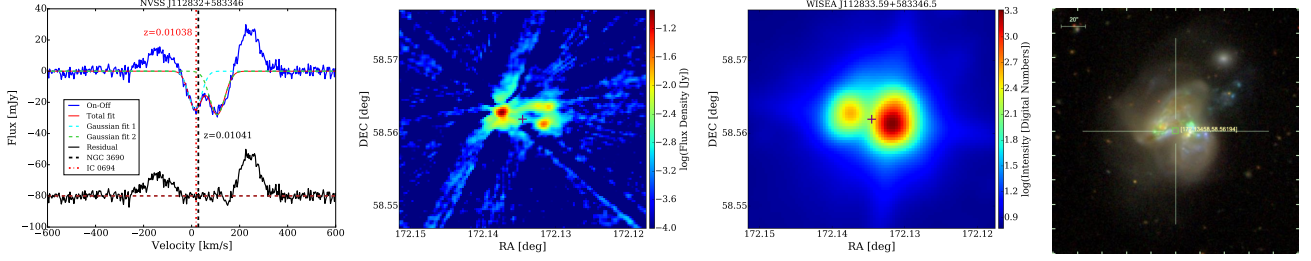


Figure 7. Left: same as Figure 3, but for NVSS J112832+583346. Middle left: radio map from VLASS centered at NVSS J112832+583346. Middle right: W2 band infrared map of WISEA J112833.59+583346.5 (WISE counterpart to NVSS J112832+583346) from WISE. Right: SDSS optical map of the optical counterpart of WISEA J112833.59+583346.5.

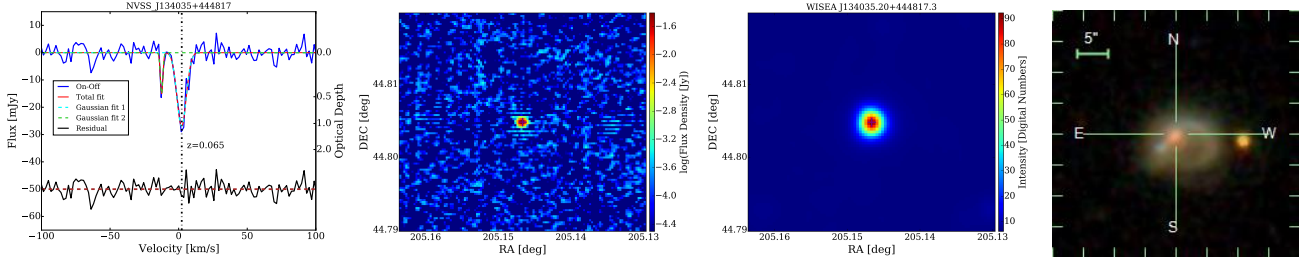


Figure 8. Left: same as Figure 3, but for NVSS J134035+444817. Middle left: radio map from VLASS centered at NVSS J134035+444817. Middle right: W2 band infrared map of WISEA J134035.20+444817.3 (WISE counterpart to NVSS J134035+444817) from WISE. Right: SDSS optical map of the optical counterpart of WISEA J134035.20+444817.3.

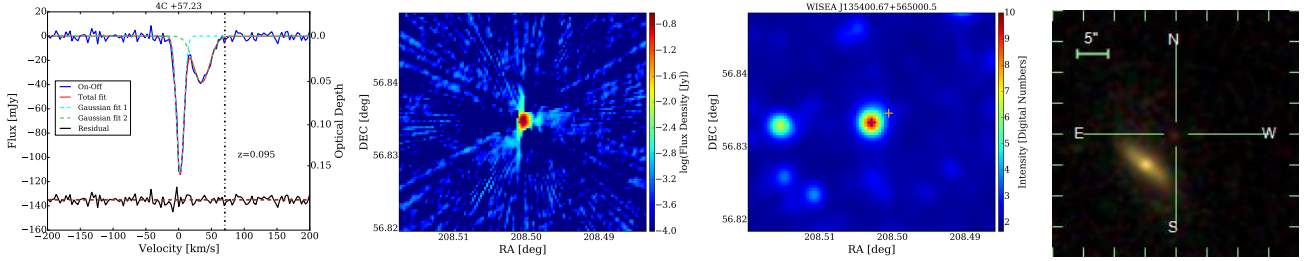


Figure 9. Left: same as Figure 3, but for 4C +57.23. Middle left: radio map from VLASS centered at 4C +57.23. Middle right: W1 band infrared map of WISEA J135400.67+565000.5 (shown as a purple cross) and 4C +57.23 (shown as an orange cross). Right: SDSS optical map centered at the optical counterpart of 4C +57.23, the bright galaxy below is the optical counterpart of WISEA J135400.67+565000.5.

NGC 5506 (Figure 10), identified as an X-ray bright Seyfert II galaxy (Wilson et al. 1976; Rubin 1978) within the local Virgo supercluster, hosts an AGN classified as a radio-quiet narrow-line Seyfert I (Nagar et al. 2002). The galaxy shows a smooth underlying stellar distribution without any apparent HII regions. Initial reports of HI absorption linked to NGC 5506 were presented by Thuan & Wadiak (1982) and subsequently mapped through a VLA imaging survey by Gallimore et al. (1999). We blindly re-detected the HI absorption associated with NGC 5506, the discerned HI profile exhibits two components: a deeper one at 1796 km s^{-1} and a shallower one at 1989 km s^{-1} . We measured the absorption with $\tau_{peak} = 0.08$ and an integrated flux of $\int S_{\text{HI}} dv = 2724.20 \text{ mJy km s}^{-1}$, which is consistent with the measurements from Gallimore et al. (1999),

where $\tau_{peak} = 0.109 \pm 0.003$ and $\int S_{\text{HI}} dv = 3.0 \pm 0.10 \text{ Jy km s}^{-1}$.

The optical image in Figure 10 reveals NGC 5506's nearly edge-on orientation, characterized by a conspicuous east-west dust lane that bisects the galaxy and a luminous, resolved nucleus, partly concealed by the dust lane. It is plausible that the predominant absorption arises from foreground disk gas, while the redshifted velocities of the line suggest that the shallower component may originate from an in-falling object.

4.1.10. NVSS J141558+132024 (PKS 1413+135)

The radio source PKS 1413+135 (Figure 11) stands out as one of the most puzzling blazars. Despite being categorized as a BL Lac object (Beichman et al. 1981; Bregman et al. 1981), PKS 1413+135 appears to

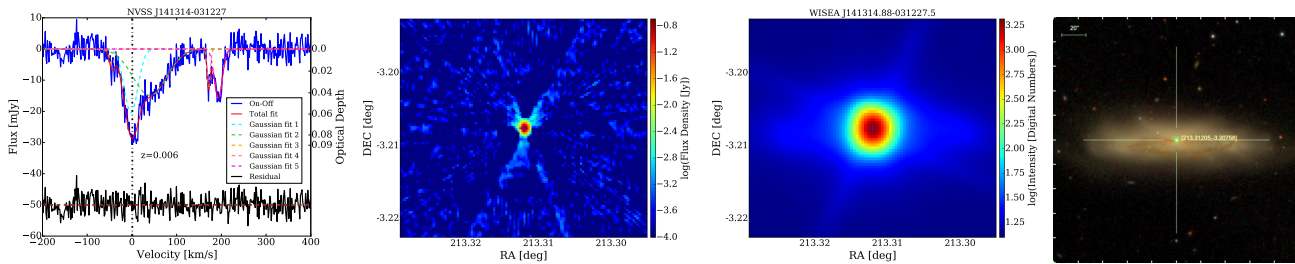


Figure 10. Left: same as Figure 3, but for NVSS J141314-031227. Middle left: radio map from VLASS centered at NVSS J141314-031227. Middle right: W2 band infrared map of WISEA J141314.88-031227.5 (WISE counterpart to NVSS J141314-031227) from WISE. Right: SDSS optical map of the optical counterpart of WISEA J141314.88-031227.5.

be linked to a disk galaxy at a redshift of 0.25 (McHardy et al. 1991). This is intriguing given that the majority of BL Lac objects and radio-loud quasars are typically associated with elliptical galaxies rather than spiral galaxies. Furthermore, while BL Lac objects usually exhibit jet axes aligned closely with the line of sight, PKS 1413+135 has also been identified as a CSO (Perlman et al. 1996). These objects have jet axes that are not aligned closely with the line of sight.

Employing multi-epoch very long baseline interferometry (VLBI), radio monitoring observations, and analyzing the infrared spectrum of PKS 1413+135, Readhead et al. (2021) demonstrated that the orientation of the jet axis closely aligns with the line of sight. The jetted AGN is highly likely to be a background source at $z < 0.5$, rather than being situated in the spiral galaxy at $z=0.247$. The intervening spiral galaxy at $z=0.247$ is identified as a Seyfert II early-type spiral galaxy, observed in an edge-on perspective.

The initial identification of HI 21 cm absorption in PKS 1413+135 was made by Carilli et al. (1992) and recently revisited with Meerkat by Combes et al. (2023). We re-detected HI absorption toward PKS 1413+135 in a blind survey and showcase its highest-resolution spectrum here. Our measurements closely align with those of Combes et al. (2023), who documented a peak optical depth of $\tau_{\text{peak}} \sim 0.463$ and $\int \tau dv = 10.86 \text{ km s}^{-1}$. The HI spectrum stands out due to its distinct narrow central component and a redshifted wing that extends up to 110 km s^{-1} . This redshifted wing is presumably associated with an outer gaseous ring orbiting the galaxy. Additionally, it has been observed that HI absorption is absent towards the radio core but is predominantly observed from a counterjet knot located 100 pc northeast of the core along the minor axis of the galaxy (Perlman et al. 2002).

From the WISE and optical image, only one source is resolved. According to the color of the WISE counterpart, this source is classified as QSOs, indicating the WISE map is dominated by the background source PKS 1413+135.

4.1.11. NVSS J160332+171158 (NGC 6034)

NGC 6034 (Figure 12) is identified as a luminous E/S0 radio galaxy within Abell 2151, which is part of the Hercules supercluster. This radio source is extended, featuring two jets emerging in the northern and southern directions. The absorption line observed in this galaxy is narrow and precisely centered at the velocity of the system, suggesting a potential HI rotating disk within the host galaxy. The presence of neutral hydrogen in NGC 6034 was initially detected through VLA observations conducted by Dickey (1997) and subsequently confirmed by the Westerbork Synthesis Radio Telescope (WSRT) observations (Geréb et al. 2015). Our independent blind detection of the HI absorption line yielded a consistent line profile, aligning with previous observations. Notably, the optical depth we obtain differs from that given in Geréb et al. (2015), mainly due to their reliance on the continuum flux measured by WSRT, which is 278 mJy, while we utilize the flux measured in the line-free region near the position of the absorption, amounting to 501.78 mJy. The FAST flux might be overestimated due to its 3-arcminute beam, which could encompass other bright sources.

4.2. New Absorbers

4.2.1. NVSS J004219+570836

NVSS J004219+570836 (Figure 13) is a blazar-like source located at $z=1.141$ and has been measured in K, Q and L band. The HI absorption profile can be modeled using a three-component Gaussian function. This function comprises a more pronounced, narrower, and symmetric component, possibly originating from the gas disk. Additionally, there are two less pronounced, broader, and redshifted components, indicating the existence of unsettled gas structures and suggesting a potential gas accretion.

4.2.2. NVSS J011322+251852

NVSS J011322+251852 (Figure 14) is a blazar-like source located at $z=1.589$ and has been measured in

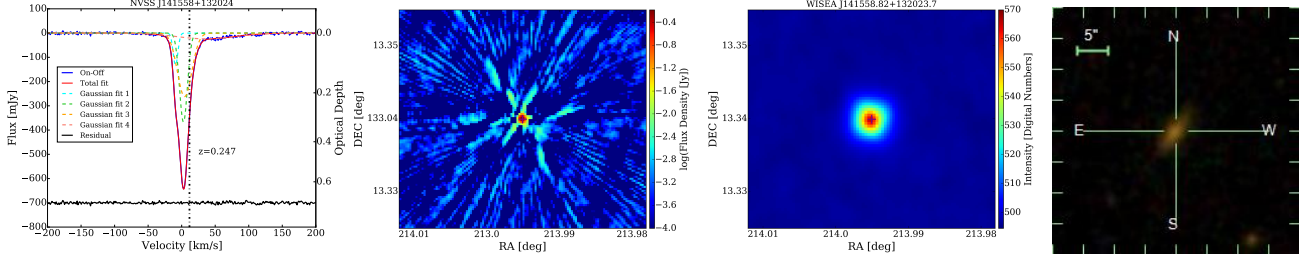


Figure 11. Left: same as Figure 3, but for NVSS J141558+132024. Middle left: radio map from VLASS centered at NVSS J141558+132024. Middle right: W3 band infrared map of WISEA J141558.82+132023.7 from WISE. Right: SDSS optical map of the optical counterpart of NVSS J141558+132024.

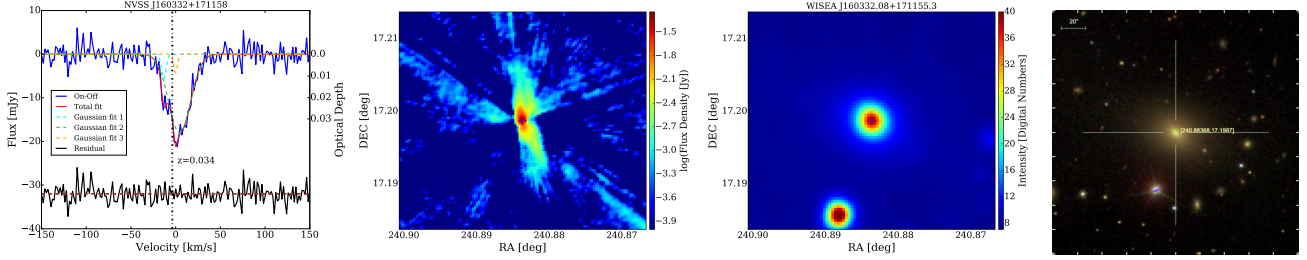


Figure 12. Left: same as Figure 3, but for NVSS J160332+171158. Middle left: radio map from VLASS centered at NVSS J160332+171158. Middle right: W2 band infrared map of WISEA J160332.08+171155.3 (WISE counterpart to NVSS J160332+171158) from WISE. Right: SDSS optical map of the optical counterpart of WISEA J160332.08+171155.3.

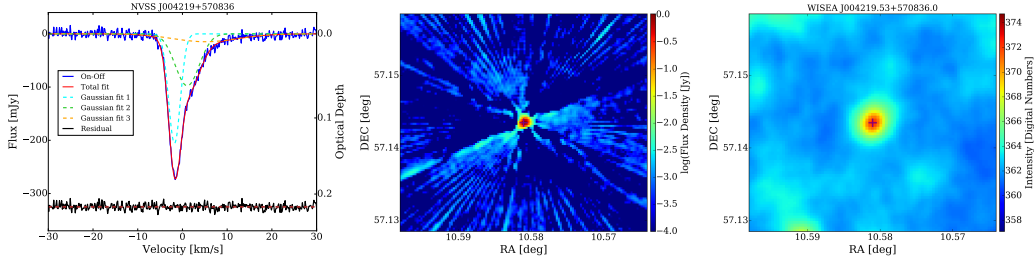


Figure 13. Left: same as Figure 2, but for NVSS J004219+570836. Middle: radio map from VLASS centered at NVSS J004219+570836. Right: WISE W3 band infrared map centred at NVSS J004219+570836.

X-ray (Burst Alert Telescope, Oh et al. 2018), ultraviolet (GALEX, Martin et al. 2005), infrared (WISE and 2MASS) and radio band (NVSS). Optical spectroscopic data is available from the SDSS-IV Extended Baryon Oscillation Spectroscopic Survey (eBOSS Myers et al. 2015). The HI absorption profile displays a more intense and symmetric component, likely stemming from the gas disk. Furthermore, a shallower redshifted wing is present, suggesting the presence of unsettled gas structures and hinting at a potential accretion of gas.

4.2.3. 4C +26.07

4C +26.07 (Figure 15) is a radio source which has been detected in the VLA Low-Frequency Sky Survey (VLSS, Cohen et al. 2007) and NVSS. Precise redshift details for 4C +26.07 are currently unavailable, resulting in uncertainty in the identification of the counterpart. A three-component Gaussian function can effectively model the

HI absorption profile. It comprises two narrower components at the center, accompanied by a broad wing signifying a possible gas disk.

4.2.4. NVSS J033529+195621

NVSS J033529+195621 (Figure 16) is a radio source which is relatively little studied. Its infrared and radio signals have been observed by WISE and NVSS. The HI absorption profile, characterized by its broad and symmetric nature, can be accurately modeled using a two-component Gaussian function.

4.2.5. NVSS J040845+001306

NVSS J040845+001306 (Figure 17) is a galaxy divided by a prominent east-west dust lane. The associated HI absorption profile comprises a broader Gaussian-shaped component and a distinct double-horn feature. The predominant absorption is likely associated with

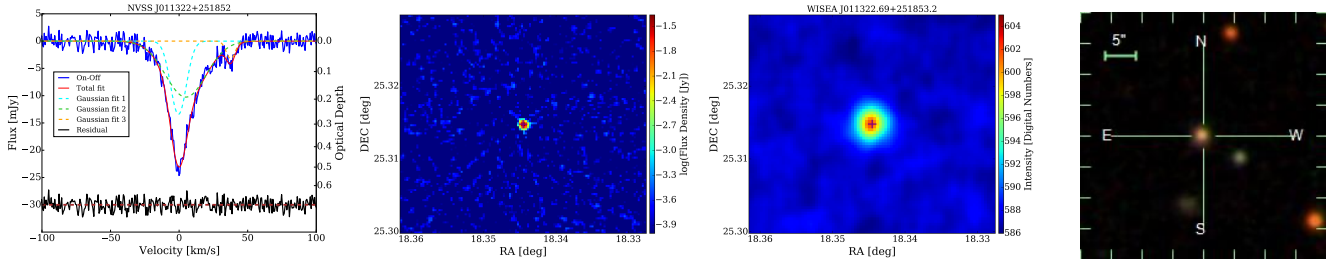


Figure 14. Left: same as Figure 2, but for NVSS J011322+251852. Middle left: radio map from VLASS centered at NVSS J011322+251852. Middle right: WISE W3 band infrared map centered at NVSS J011322+251852. Right: SDSS optical map centered at NVSS J011322+251852.

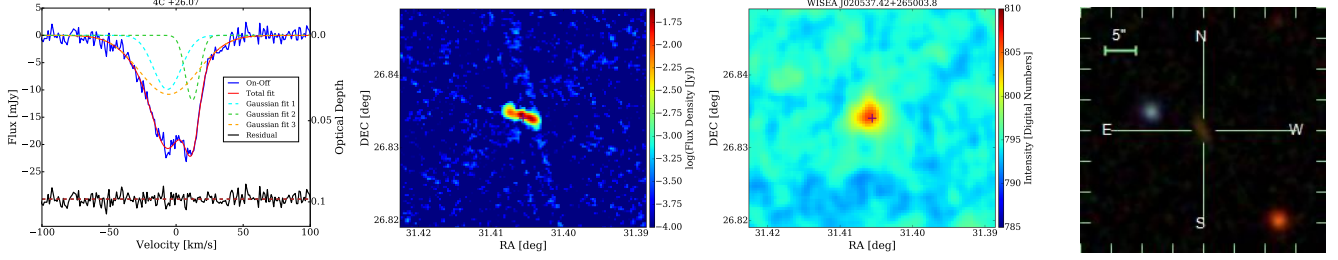


Figure 15. Left: same as Figure 2, but for 4C+26.07. Middle left: radio map from VLASS centered at 4C+26.07. Middle right: WISE W3 band infrared map centered at 4C+26.07. Right: SDSS optical map of the optical counterpart of 4C+26.07.

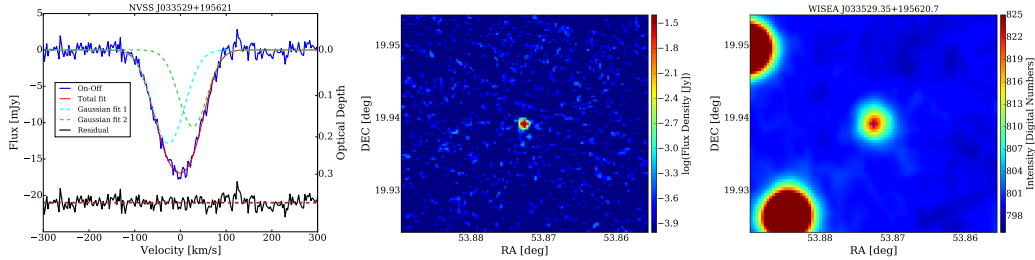


Figure 16. Left: same as Figure 2, but for NVSS J033529+195621. Middle: radio map from VLASS centered at NVSS J033529+195621. Right: WISE W3 band infrared map centered at NVSS J033529+195621.

diffuse gas, while the sharp component may stem from gas in rotational motion within the galaxy.

4.2.6. NVSS J055437+271126

NVSS J055437+271126 (Figure 18) is a radio source, detected in NRAO VLA Sky Survey and re-detected in mid-infrared band in WISE Survey and Two Micron All Sky Survey (2MASS, *Skrutskie et al. 2006*). Only a photometric redshift with a large uncertainty is available. The HI absorption profile is wide and symmetrical, which can be properly modeled using a three-component Gaussian function.

4.2.7. NVSS J073755+264652

NVSS J073755+264652 (Figure 19) is a blue radio galaxy that has been observed in ultraviolet (GALEX), optical (SDSS), infrared (WISE and 2MASS) and radio band (NVSS). The HI absorption profile demonstrates straightforward symmetry and can be precisely repre-

sented by a one-component Gaussian function. This suggests the existence of a settled system with a gas disk.

4.2.8. NVSS J080101-075121

NVSS J080101-075121 (Figure 20) has been detected at 365 MHz in the Texas Survey of Radio Sources (*Douglas et al. 1996*) and at 1.4 GHz in NVSS, and it is detected in the mid-infrared band by WISE. The absence of redshift for the radio source NVSS J080101-075121 introduces uncertainty in identifying the counterpart in the foreground/background. The W1-W2 color of NVSS J080101-075121 is 0.135, which is lower than the value of 0.8 often used to select AGN candidates, and implies that the mid-IR emission comes mainly from stars. Combined with the W2-W3 value of 2.617 mag, NVSS J080101-075121 lies in the region of spiral galaxies in the WISE color-color diagram.

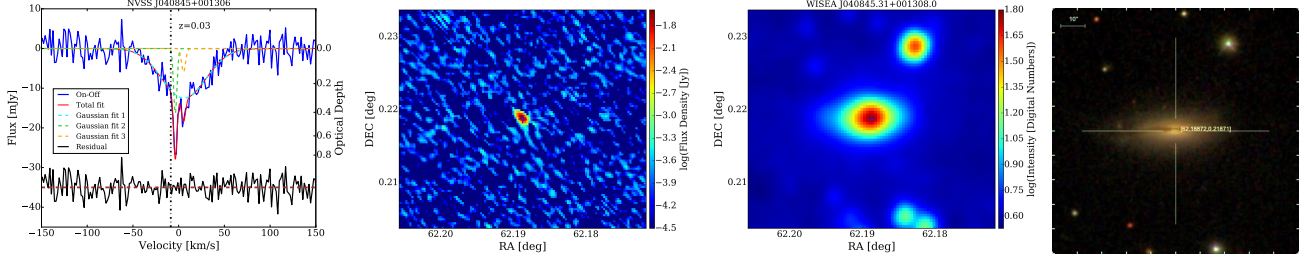


Figure 17. Left: same as Figure 3, but for NVSS J040845+001306. Middle left: radio map from VLASS centered at NVSS J040845+001306. Middle right: W1 band infrared map of WISEA J040845.31+001308.0. from WISE. Right: SDSS optical map of the optical counterpart of WISEA J040845.31+001308.0.

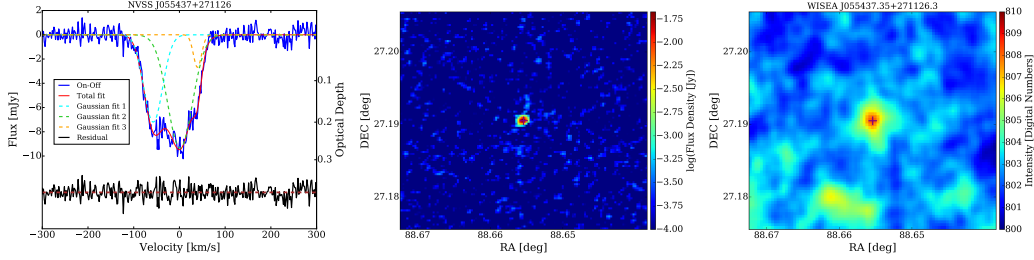


Figure 18. Left: same as Figure 2, but for NVSS J055437+271126. Middle: radio map from VLASS centered at NVSS J055437+271126. Right: WISE W3 band infrared map centered at NVSS J055437+271126.

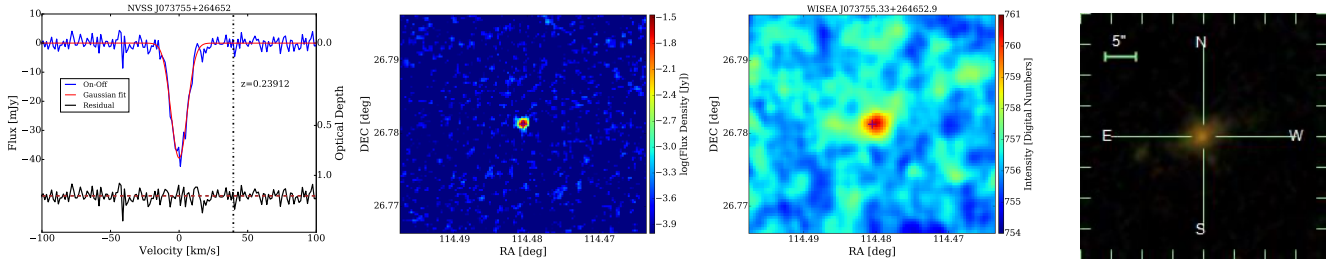


Figure 19. Left: same as Figure 3, but for NVSS J073755+264652. Middle left: radio map from VLASS centered at NVSS J073755+264652. Middle right: W3 band infrared map of WISEA J073755.33+264652.9 from WISE. Right: SDSS optical map of the optical counterpart of NVSS J073755+264652.

The HI absorption profile reveals a symmetric, broader component, likely associated with the gas disk, and a narrower, deeper peak, suggesting the presence of distinct, unsettled gas structures.

4.2.9. NVSS J092351+281527

Positioned at a redshift of 0.745, NVSS J092351+281527 (Figure 21), identified as a quasar, has undergone observations across various spectra, including ultraviolet (GALEX), optical (SDSS), Infrared/Submillimeter (WISE and Planck), and radio bands (Texas, FIRST, and NVSS). Additionally, NVSS J092351+281527 is categorized as a Flat-Spectrum Radio Source in Healey et al. (2007). The counterpart to the foreground is currently ambiguous, necessitating high-resolution follow-up observations for verification.

4.2.10. NVSS J093150+254034

NVSS J093150+254034 (Figure 22) is a galaxy located at a redshift of 0.812, which has been observed in infrared (WISE) and radio bands (NVSS). The counterpart to the foreground is currently uncertain. The HI absorption profile from this intervening system exhibits a slender and symmetrical shape, suggesting the presence of a gas disk.

4.2.11. NVSS J094208+135152

NVSS J094208+135152 (Figure 23) is categorized as a radio source, close to 3C 225A (located at $z = 1.565$), with a mere 0.039 arcmin separation. Since only one radio source is identified in the same region by VLASS, NVSS J094208+135152 likely corresponds to 3C 225A. In the HUBBLE SPACE TELESCOPE snapshot survey presented by McCarthy et al. (1997), the identification of 3C 225A is very faint and is confused with a foreground spiral in ground-based images. The SDSS coun-

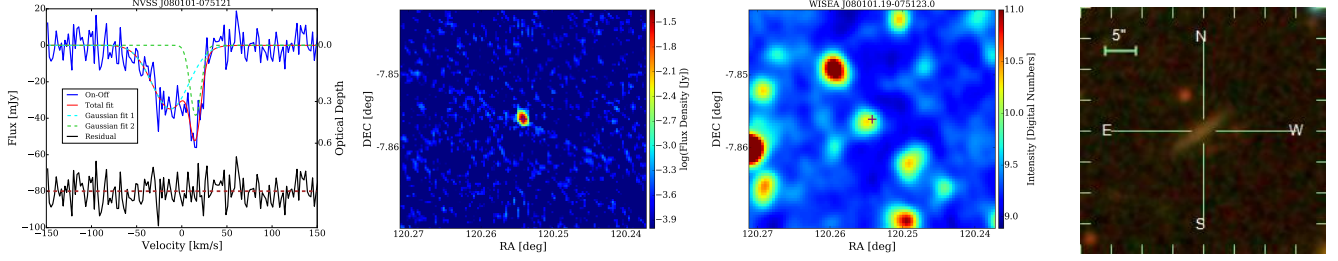


Figure 20. Left: same as Figure 2, but for NVSS J080101-075121. Middle left: radio map from VLASS centered at NVSS J080101-075121. Middle right: WISE W2 band infrared map centered at NVSS J080101-075121. Right: SDSS optical map centered at NVSS J080101-075121.

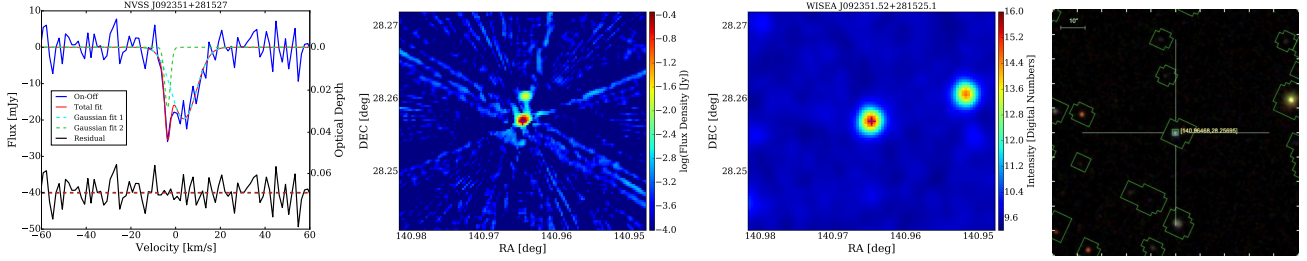


Figure 21. Left: same as Figure 2, but for NVSS J092351+281527. Middle left: radio map from VLASS centered at NVSS J092351+281527. Middle right: W2 band infrared map centered at NVSS J092351+281527. Right: SDSS optical map centered at NVSS J092351+281527.

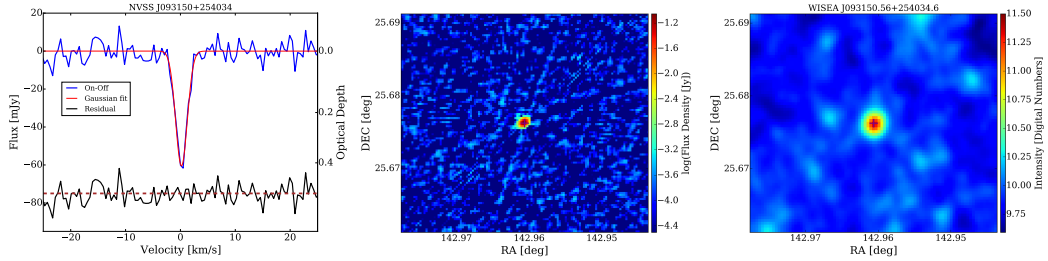


Figure 22. Left: same as Figure 2, but for NVSS J093150+254034. Middle: radio map from VLASS centered at NVSS J093150+254034. Right: WISE W2 band infrared map centered at NVSS J093150+254034.

terpart to the foreground galaxy is SDSS J094208.05+135154.9, its magnitudes are $u=20.724$, $g=19.471$, $r=18.889$, $i=18.614$ and $z=18.536$.

The WISE counterpart to foreground galaxy SDSS J094208.05+135154.9 is WISEA J094208.11+135155.0 as shown in the NED. The WISE W1[3.4 μm], W2[4.6 μm], W3[12.1 μm] and W4[22.2 μm] magnitudes for WISEA J094208.11+135155.0 are 16.307 ± 0.101 , 15.839 ± 0.225 , 11.331 ± 0.173 and 8.316 , respectively. The W1-W2 color of WISEA J094208.11+135155.0 is 0.468, which means that the mid-IR emission comes mainly from the stars. According to the W2-W3 value of 4.508 mag, WISEA J094208.11+135155.0 is located in the ULIRGs/LINERs region in the WISE color-color diagram.

4.2.12. NVSS J095058+375758

NVSS J095058+375758 (Figure 24) is a nearby galaxy hosting AGN. Morphologically, it is classified as an edge-on FR0 galaxy (Ma et al. 2019). The associated HI absorption profile shows symmetry, indicating a gas disk, as the absorption line is centered at the systemic velocity of the galaxy.

4.2.13. NVSS J095812+112643

NVSS J095812+112643 (Figure 25) is a radio galaxy that has been observed in optical (SDSS), infrared (WISE) and radio band (NVSS, VLSS, and Texas (Douglas et al. 1996)). The lack of precise redshift information for NVSS J095812+112643 gives rise to uncertainty regarding its status in the foreground or background. The HI absorption profile observed in this system displays a slim and symmetrical shape, indicating the likely presence of a gas disk.

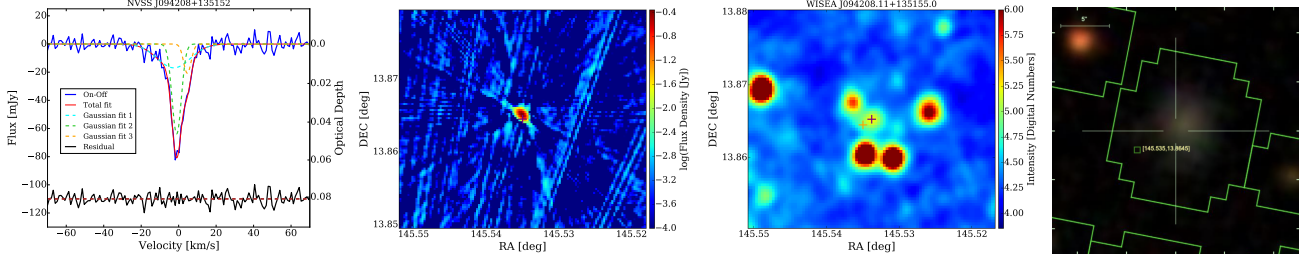


Figure 23. Left: same as Figure 2, but for NVSS J094208+135152. Middle left: radio map from VLASS centered at NVSS J094208+135152. Middle right: W1 band infrared map centered at WISEA J094208.11+135155.0 (shown as a purple cross). The position of the background is shown as an orange cross). Right: SDSS optical map of the SDSS J094208.05+135154.9. The green square shows the position of the background radio source.

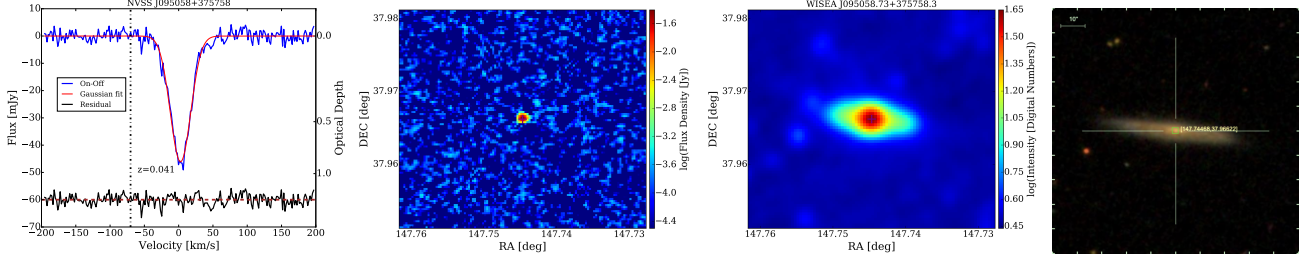


Figure 24. Left: same as Figure 3, but for NVSS J095058+375758. Middle left: radio map from VLASS centered at NVSS J095058+375758. Middle right: W1 band infrared map of WISEA J095058.73+375758.3. from WISE. Right: SDSS optical map of the optical counterpart of WISEA J095058.73+375758.3.

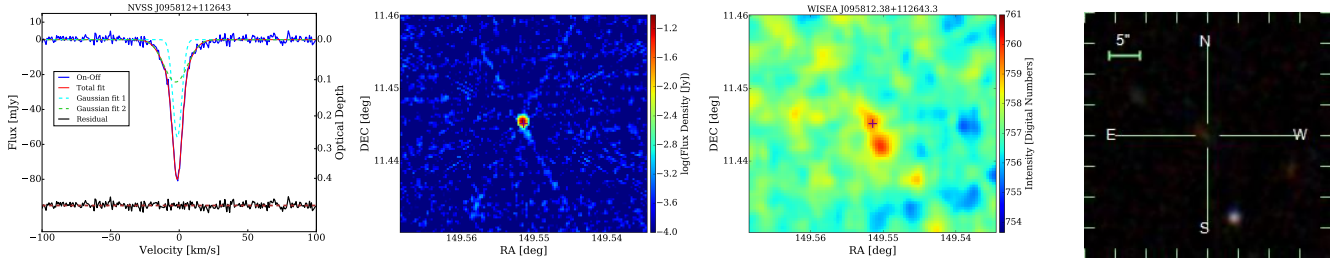


Figure 25. Left: same as Figure 2, but for NVSS J095812+112643. Middle left: radio map from VLASS centered at NVSS J095812+112643. Middle right: WISE W3 band infrared map centered at NVSS J095812+112643. Right: SDSS optical map centered at NVSS J095812+112643.

4.2.14. NVSS J100755+405519

NVSS J100755+405519 (Figure 26) is a radio source, detected in the Faint Images of the Radio Sky at Twenty Centimeters Survey (FIRST, Becker et al. 1995) and NVSS. WISE and SDSS measured its flux density in the mid-infrared band and optical band, respectively. Precise redshift information for NVSS J100755+405519 is currently unavailable, making it difficult to determine whether it is an associated or intervening system.

The WISE counterpart to NVSS J100755+405519 is WISEA J100755.72+405517.7 according to the NED. The W1-W2 color of WISEA J100755.72+405517.7 is 1.005, indicating WISEA J100755.72+405517.7 is an AGN candidate. Combined with the W2-W3 value of

3.074 mag, WISEA J100755.72+405517.7 is located in the region of QSOs in the WISE color-color diagram.

The intricate absorption profile suggests an unsettled system. To characterize this profile, a seven-component Gaussian function is employed. Apart from dominant components at the center, three components exhibit blueshifts with velocity separations of -73 km/s, -46 km/s, and -36 km/s, suggesting a potential gas outflow or the presence of a satellite galaxy. Additionally, a redshifted component implies the possibility of gas accretion.

4.2.15. NVSS J104941+133255

NVSS J104941+133255 (Figure 27) is a quasar located at a redshift of 2.764, it has been observed in optical and Ultraviolet (SDSS), and radio bands (NVSS and

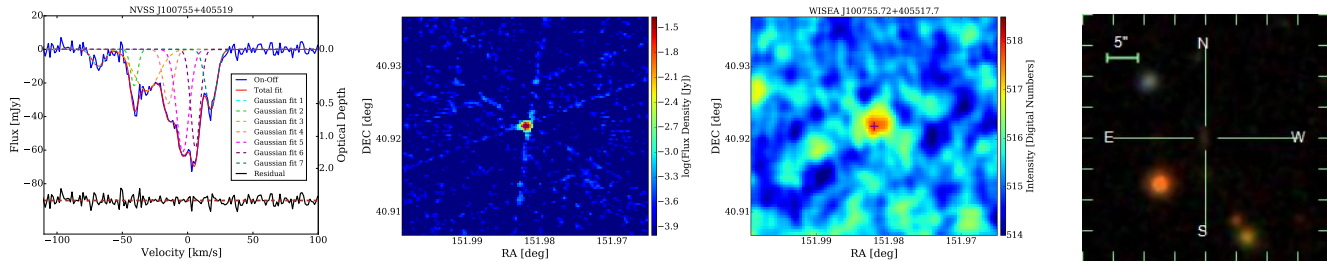


Figure 26. Left: same as Figure 2, but for NVSS J100755+405519. Middle left: radio map from VLASS centered at NVSS J100755+405519. Middle right: WISE W3 band infrared map centered at NVSS J100755+405519. Right: SDSS optical map of the optical counterpart of NVSS J100755+405519.

Texas Survey). The foreground object remains ambiguous and requires a thorough high-resolution follow-up observation for confirmation. The HI absorption profile exhibits symmetry and can be accurately modeled using a one-component Gaussian function.

4.2.16. NVSS J115948+582020

NVSS J115948+582020 (Figure 28) is a quasar located at $z=0.629$ and has been observed in optical (eBOSS), infrared (WISE), and radio bands (NVSS, VLBA and Texas Survey). The HI absorption signal in this intervening system is robust, displaying an almost symmetrical shape that can be effectively modeled using a three-component Gaussian function.

4.2.17. NVSS J162549+402921 (NGC 6150)

NGC 6150 (Figure 29) is situated within the Abell 2197 cluster and is classified as an elliptical galaxy (Nair & Abraham 2010). As documented by O’Dea et al. (1987), NGC 6150 is identified as a narrow-angle tail (NAT) radio source.

4.2.18. NVSS J225900+274356

NVSS J225900+274356 (Figure 30) is an AGN-host radio galaxy with a phot $z=0.110 \pm 0.0236$, which has been observed in the Infrared/Submillimeter (WISE and 2MASS) and radio bands (Texas and NVSS). The photometric redshift is lower than the redshift of the HI absorption, suggesting that the HI gas might originate from an associated infalling object.

The HI absorption profile exhibits a symmetric, narrower, and more intense component, likely originating from a gas disk. Additionally, there is a broader, shallower redshifted wing, indicating the existence of unsettled gas structures and a potential accretion of gas onto the SMBH.

5. HI ABSORPTION PROPERTIES

5.1. HI Absorption Statistics

Physical properties of associated and intervening absorption are investigated in this section, to understand

the nature of HI absorption systems. We also place our results within the broader context of previous and ongoing HI 21-cm absorption surveys, including the detections of FLASH (Allison et al. 2020; Sadler et al. 2020; Mahony et al. 2022; Weng et al. 2022; Su et al. 2022; Aditya et al. 2024), MALS (Srianand et al. 2022; Maina et al. 2022; Deka et al. 2024a) and of the surveys using WSRT (Geréb et al. 2015; Maccagni et al. 2017), the Giant Metrewave Radio Telescope (GMRT, Kanekar et al. 2009; Gupta et al. 2009, 2012; Aditya & Kanekar 2018a,b; Aditya 2019; Chandola et al. 2020; Aditya et al. 2021) and FAST (Chandola et al. 2024).

5.1.1. HI absorption surveys

Using WSRT, Geréb et al. (2015); Maccagni et al. (2017) detected 66 associated HI absorption in 248 radio sources at $0.02 < z < 0.25$. These sources were selected by cross-correlating the SDSS DR7 with the FIRST catalog, applying a flux density threshold of $S_{1.4GHz} > 30$ mJy. Aditya (2019) observed a sample of 11 radio-bright galaxies, also selected by cross-correlating the SDSS DR7 with the FIRST catalog, using the Band-4 of upgraded GMRT (covering $0.7 < z < 1.0$), resulting in the detection of four associated HI 21-cm absorption systems. Aditya & Kanekar (2018b) presented 16 associated HI absorption systems in 92 AGNs at $z < 3.6$, from the Caltech–Jodrell Bank flat-spectrum (CJF) sample. Additionally, the results of HI 21-cm absorption searches in 30 GPS sources, including 14 associated detections, are presented in Aditya & Kanekar (2018a). Chandola et al. (2020) presented seven associated detections from HI absorption experiment conducted using the GMRT towards 27 low- and intermediate-luminosity AGNs, classified as either low excitation radio galaxies (LERGs) or high excitation radio galaxies (HERGs), with WISE color $W2[4.6\mu m]-W3[12\mu m]>2$. Chandola et al. (2024) reported eight associated HI 21-cm absorption detections from a HI and OH absorption survey conducted with FAST. This survey targeted 40 radio sources with low-to-intermediate radio luminosity, red mid-infrared colors $(W2[4.6\mu m] - W3[12\mu m])>2.5$

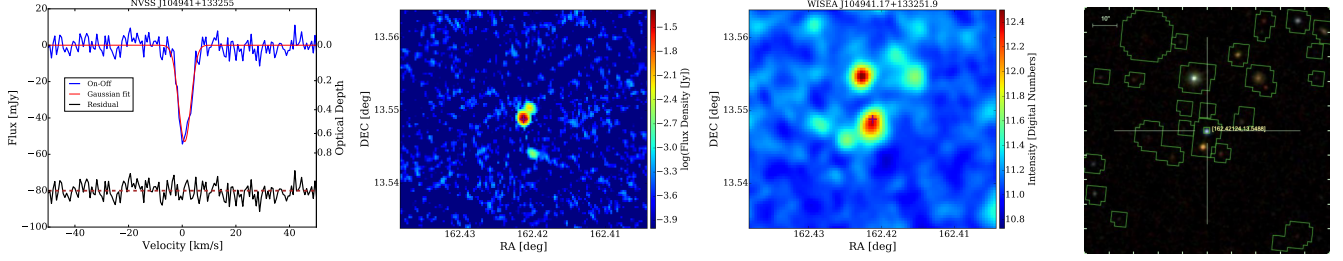


Figure 27. Left: same as Figure 2, but for NVSS J104941+133255. Middle left: radio map from VLASS centered at NVSS J104941+133255. Middle right: WISE W2 band infrared map centered at NVSS J104941+133255. Right: SDSS optical map centered at NVSS J104941+133255. The bright orange point source below NVSS J104941+133255 is a star.

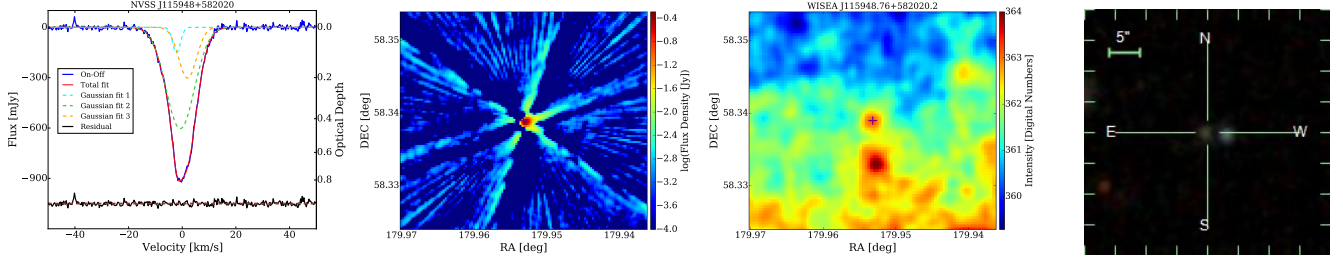


Figure 28. Left: same as Figure 2, but for NVSS J115948+582020. Middle left: radio map from VLASS centered at NVSS J115948+582020. Middle right: WISE W3 band infrared map centered at NVSS J115948+582020. Right: SDSS optical map centered at NVSS J115948+582020.

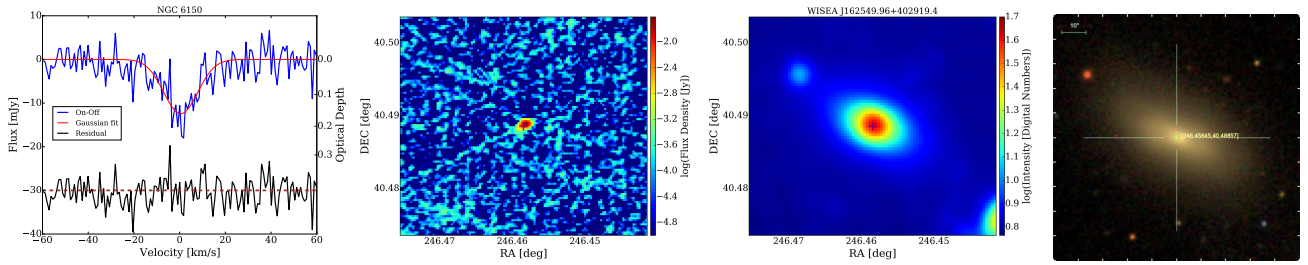


Figure 29. Left: same as Figure 2, but for NGC 6150. Middle left: radio map from VLASS centered at NGC 6150. Middle right: W2 band infrared map centered at NGC 6150. Right: SDSS optical map of the SDSS J162549.96+402919.3.

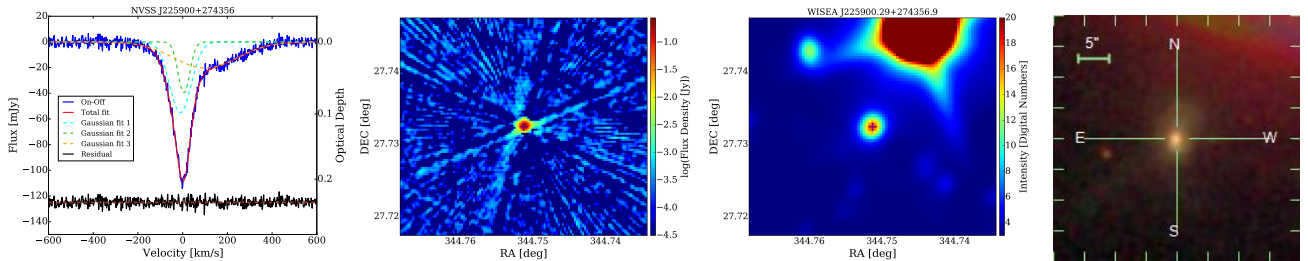


Figure 30. Left: same as Figure 3, but for NVSS J225900+274356. Middle left: radio map from VLASS centered at NVSS J225900+274356. Middle right: W1 band infrared map of WISEA J225900.29+274356.9. from WISE. Right: SDSS optical map of the optical counterpart of WISEA J225900.29+274356.9.

mag), and redshifts up to 0.35. Moreover, several high-redshift intervening and associated HI 21-cm absorptions were recently detected in the FLASH and MALS surveys. Moreover, for the survey of intervening 21-cm absorption, Kanekar et al. (2009) and Gupta et al. (2009,

2012) utilized the GMRT to search for HI 21-cm absorption in strong Mg II absorbers within the redshift range $0.5 < z < 1.5$, yielding 18 detections of intervening systems.

A total of 116 associated and 24 intervening HI 21-cm absorption systems from previous and ongoing HI 21-cm absorption surveys are combined with our catalog to analyze the physical properties of HI absorption. We retrieve 1.4 GHz flux density, morphology data, WISE magnitudes, and SDSS magnitudes from the NVSS, VLASS, WISE, and SDSS (or from Pan-STARRS (Chambers et al. 2016) if the source is not covered by SDSS) surveys, respectively. In some cases, HI absorption may lack counterparts in these surveys due to incomplete sky coverage or insufficient redshift information. In each of the following sections, we exclude HI absorption systems where the necessary data are unavailable.

5.1.2. Distribution in Redshift

In Figure 31 we plot the redshift versus 1.4-GHz flux density of the radio sources for HI absorption systems (upper panel) and HI column density (lower panel), along with their corresponding histograms for HI absorption systems across all considered samples. For the HI absorption detected in this work, the scarcity of HI absorption systems found between redshift 0.136 and 0.235 is attributed to interference caused by RFIs in the frequency range from 1150 MHz to 1250 MHz. For both intervening and associated HI absorption systems, there are no evident correlations between redshift and flux densities of radio sources for HI absorption systems, nor between redshift and N_{HI} . An intriguing result from the distribution of HI absorption across redshifts reveals a significant dichotomy: the majority of detected associated HI absorption systems are found at lower redshifts ($z < 0.20$), whereas detected intervening HI absorption systems predominantly occur at higher redshifts ($z > 0.2$). This highlights a clear separation in redshift distribution between associated and intervening systems. This phenomenon can be explained by the lower probability of encountering an intervening absorber at a low redshift and the increased difficulty in identifying an absorber as associated at a higher redshift. At low redshifts, the lower density of intervening systems results in a lower probability of encountering absorbers, while at high redshifts, the difficulty in identifying associated absorbers stems from observational challenges and the complex nature of high-redshift environments.

To investigate the properties of HI absorption at various redshifts, we set a redshift threshold of 0.5 (black-dashed line in Figure 31) in the following sections, dividing the absorption systems into two categories: high-redshift and low-redshift samples.

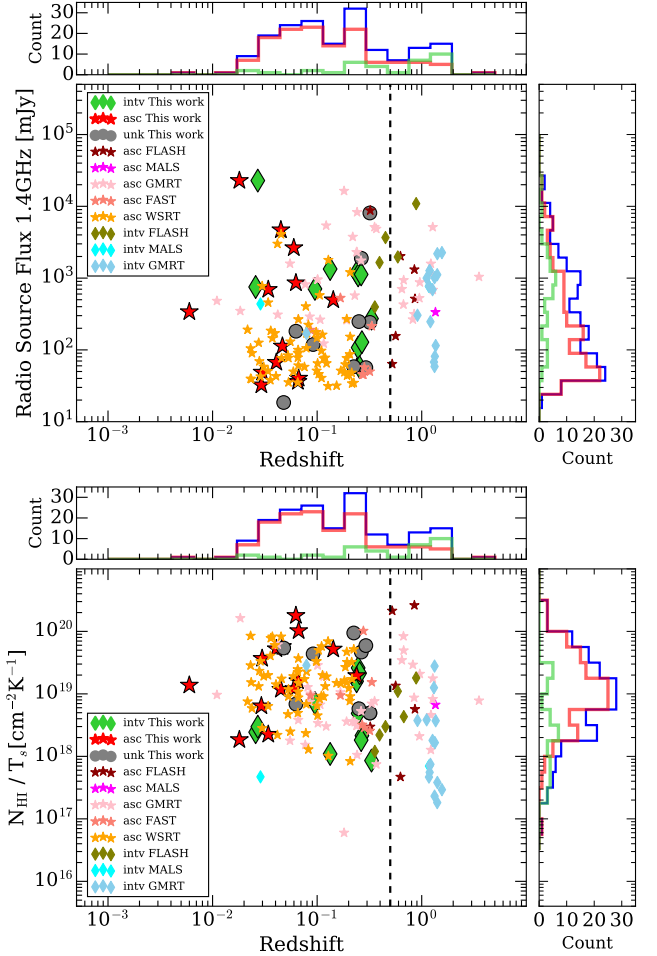


Figure 31. Redshift versus 1.4-GHz flux density of radio sources for the HI absorption systems (upper) and HI column density (lower). The black dashed line represents the redshift threshold of 0.5, which we used to distinguish between the higher- and lower-redshift samples discussed in the following sections.

5.1.3. integrated column density versus flux density of radio sources

The relationship between integrated HI column density and 1.4-GHz flux density of radio sources for HI absorption systems we detected, along with their corresponding histograms and those for HI absorption systems reported in the literature, is shown in Figure 32. The flux densities of radio sources for HI absorption systems we detected span a large range, from ~ 20 mJy to ~ 23 Jy. When comparing intervening and associated systems in our sample, the flux density of radio sources within associated systems exhibits a wider range in both very low (flux ≤ 60 mJy) and high (flux ≥ 2 Jy) flux density regions. In terms of HI column density, associated systems exhibit higher values compared to intervening systems. These patterns are also observed in the

relationship between integrated HI column density and 1.4-GHz flux density of radio sources in HI absorption systems of all considered surveys outlined at the beginning of Section 5.1. Given that the associated systems are typically found at the center of AGNs while the intervening systems are usually associated with spiral galaxies, our measurements suggest that intervening systems may only trace part of the gas, whereas associated systems may capture the entirety of gas components.

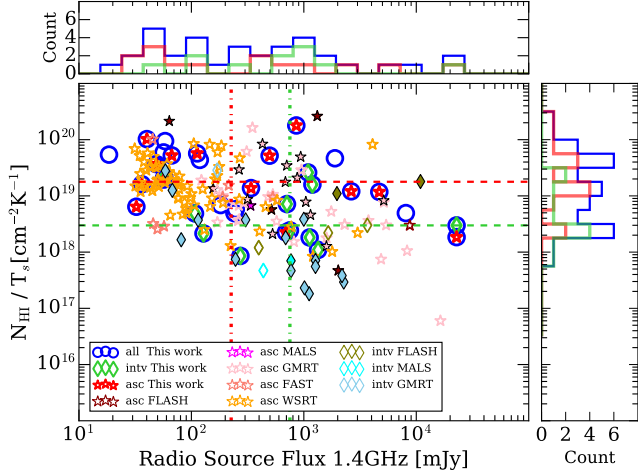


Figure 32. HI column density versus 1.4-GHz flux density of radio sources for both the HI absorption systems we detected and those reported in the literature. Higher- ($z > 0.5$) and lower-redshift ($z \leq 0.5$) samples are represented by filled points and open points, respectively. Dashed and dot-dashed lines represent median values for intervening (green diamond) and associated (red star) systems detected in this work, respectively.

5.1.4. Column Density versus FWHM

Figure 33 illustrates the correlation between HI column density and FWHM of HI absorption systems. The FWHM values for intervening systems are significantly lower compared to those of associated systems, this is because an intervening galaxy in HI absorption may be traced only partially and produce narrower lines. For the systems detected in this work, the median FWHM for intervening systems is $9.00 \pm 6.11 \text{ km s}^{-1}$, whereas for associated systems, it is $44.90 \pm 106.05 \text{ km s}^{-1}$. Furthermore, there is a noticeable trend indicating that HI column density increases with FWHM, with this pattern being more pronounced for associated systems compared to intervening systems.

5.1.5. Column Density versus Morphology

Enhancing our comprehension of the gas properties associated with different radio source types, such as com-

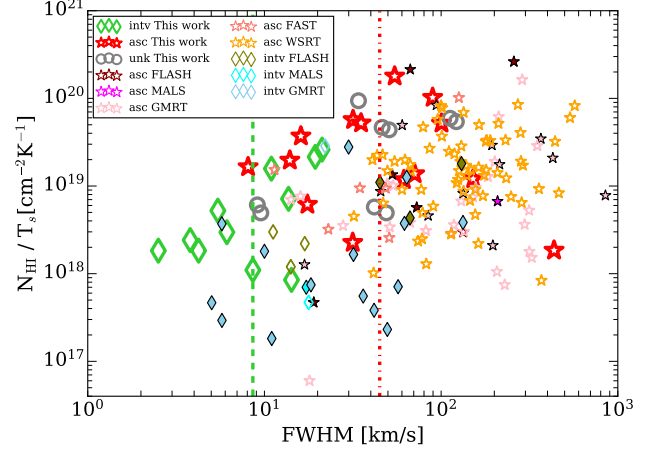


Figure 33. The HI column density versus FWHM for both our sample and the sample from the literature. Higher- ($z > 0.5$) and lower-redshift ($z \leq 0.5$) samples are represented by filled points and open points, respectively. The green and red dashed lines indicate the median values for the intervening and associated systems detected in this study.

compact and extended, is vital for understanding the observed features of AGNs. Furthermore, it is proposed that AGN of different types are encased in different gaseous environments and exhibit divergent HI detection rates. Geréb et al. (2014) analyzed a sample of 93 AGNs, selected based on a flux criterion ($S_{1.4\text{GHz}} > 50 \text{ mJy}$) and having SDSS redshifts in the range $0.02 < z < 0.23$, categorizing them into compact and extended radio sources. They discovered that the compact sources (with $g - r > 0.7$) exhibit an HI absorption detection rate of approximately 42%, in contrast to just about 16% for extended sources. Through a stacking analysis, it was revealed that the HI absorption associated with the compact radio sources typically presents higher optical depth, FWHM, and HI column densities compared to those linked with extended sources (Geréb et al. 2014). Furthermore, Geréb et al. (2015) reported a tendency for HI absorption features in compact radio sources to display blueshifted and broad/asymmetric line profiles more frequently. Additionally, Maccagni et al. (2017) reported that compact sources exhibit broad HI lines, indicating unsettled kinematics. Both Maccagni et al. (2017) and Chandola & Saikia (2017) further noted a higher detection rate of HI absorption in compact sources compared to extended sources. More recently, Aditya et al. (2024) presented an ASKAP pilot search for associated HI 21-cm absorption in a sample of 62 Molonglo Reference Catalog 1-Jy radio galaxies and quasars covering $0.42 < z < 1.00$, identifying three new detections of associated HI 21-cm absorption, all

of which were from peaked-spectrum or compact steep-spectrum radio sources.

We explore N_{HI} levels in HI absorption associated with radio sources of varying morphologies in our sample. The morphology is characterized by metrics such as the minor-to-major axis ratio, the peak-to-integrated flux ratio, and the peak-to-ring flux ratio (defined as the ratio of maximum brightness within 5 arcsecs of the component to the maximum brightness in an annulus centered on the component with inner and outer radii of 5 arcsecs and 10 arcsecs). These parameters were obtained from the VLASS catalog. Radio sources (4C -06.18 and 3C 84) located outside the VLASS coverage area were omitted from the morphology-based analysis. The findings are depicted in Figure 34. For intervening systems, there appears to be no discernible connection between the morphology of background radio sources and N_{HI} . Similarly, for associated systems, no evident relationship is observed between the minor-to-major axis ratio and N_{HI} . However, there are noticeable increasing trends of N_{HI} with both the peak-to-integrated flux ratio and the peak-to-ring flux ratio, suggesting that associated HI absorption linked to compact radio sources exhibits higher HI column densities in comparison to those associated with extended radio sources.

5.1.6. Column Density versus Color

The N_{HI} versus the SDSS $g-r$ color of our HI 21-cm absorption sample, along with those of HI absorption systems reported in the literature, is shown in Figure 35. For both the associated HI absorption in our sample and the literature, most of the hosting galaxies are red ($g-r > 0.7$) objects. The background sources in the intervening systems within our sample span a wide range of $g-r$ color values, whereas most background sources reported in the literature fall within the blue object region ($g-r < 0.7$). Among the three intervening systems in our sample with identified foreground sources, two are classified as blue objects. Out of the five identified foreground sources from our sample and literature, three are also blue objects. A preliminary division in color distribution for foregrounds of intervening and associated systems has been identified, necessitating further validation with a larger sample size, especially concerning intervening systems. This division aligns with the redshift distribution of associated and intervening HI absorption detailed in Section 5.1.2, reflecting the prevalence of bluer galaxies at higher redshifts due to the process of galaxy evolution. The small sample size of the identified foreground objects in the intervening system in the literature limits the ability to draw a high-confidence conclusion. For the associated systems, those at higher

redshift ($z > 0.5$) show less concentration along the color axis and exhibit a broader range of $g-r$ colors.

Figure 35 illustrates that only a small fraction of intervening absorption systems have identified foreground sources. Identifying these foreground objects is challenging because their signal is often obscured by the intense signal of the bright background. A blind radio survey can assist in detecting intervening absorption systems with backgrounds that are less bright in the optical band.

5.2. WISE color-color Classification

The WISE color-color diagram is often used to illustrate the locations of interesting classes of objects and has also been employed to classify HI 21-cm absorption. Chandola & Saikia (2017) identified a clear distinction in the W2-W3 color distributions between sources with and without HI detections, with detections having larger W2-W3 values than non-detections. They also observed a high detection rate of HI absorption in galaxies with WISE infrared colors $W2-W3 > 2$, which are typically gas-rich systems and possess compact radio structures. Maccagni et al. (2017) used WISE colors to differentiate between dust-poor sources and mid-infrared (MIR) bright sources. They found that dust-poor galaxies predominantly exhibit narrow, deep HI absorption lines, usually centered at the systemic velocity, indicating that most HI in these galaxies is settled in a rotating disk. In contrast, MIR bright sources showed more frequent HI detections compared to dust-poor sources.

We use the WISE color to infer possible classes of foreground and background sources, the positions of our systems in the color-color diagram are shown in Figure 36. Among the intervening systems we detected, eight background radio sources have corresponding WISE counterparts. Of these, five are located in the region of QSOs, while two are found in areas corresponding to either spiral or elliptical galaxies. Almost all the background radio sources in the intervening systems in the quoted GMRT survey position in the QSOs region. These findings are further supported by the discoveries from GMRT, FLASH, and MALS. Additionally, four (including the one from FLASH) foreground radio sources in the intervening systems were identified in the WISE survey, each in distinct regions: three in a spiral galaxy, and the fourth in the ULIRGs/LINERs starburst region. For the associated systems, the radio sources spread a broader range of locations, encompassing the QSO region, Seyferts region, spiral galaxy region, elliptical galaxy region, and the ULIRGs/LINERs starburst region, with the spiral galaxy region representing the largest portion. This distribution pattern is consistent

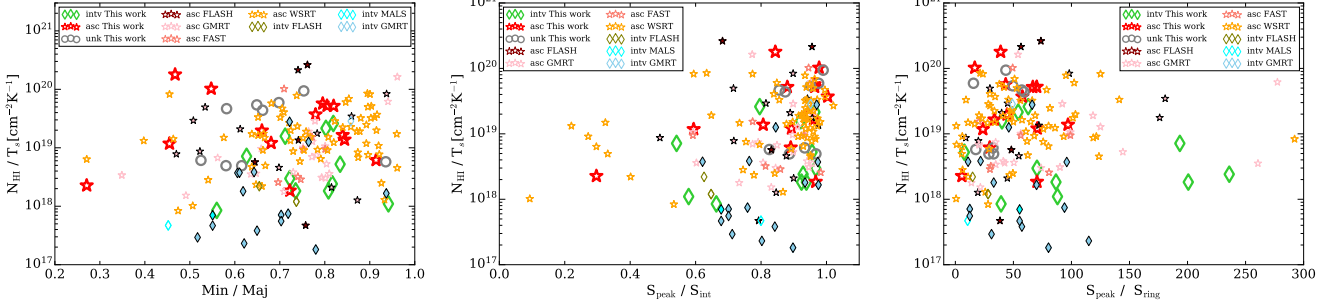


Figure 34. Same as Figure 33, but for the minor-to-major axis ratio (left), peak-to-integrated flux ratio (center), and peak-to-ring flux ratio (right) versus HI column density.

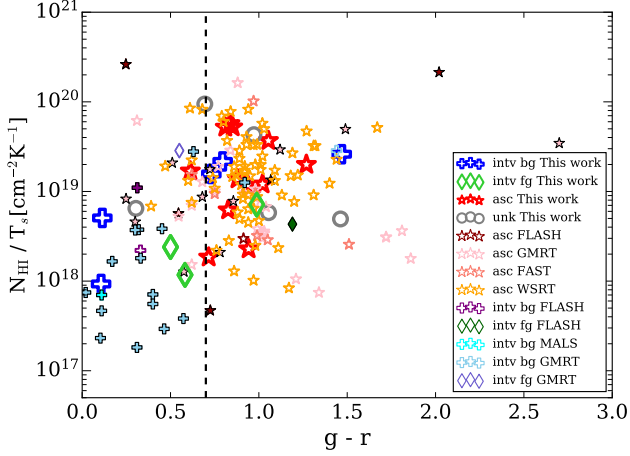


Figure 35. Same as Figure 33, but for the HI column density versus the SDSS $g-r$ color. The black-dashed line represents a $g-r$ value of 0.7.

in both our sample and those reported in the literature. Literature detections indicate that the distribution of associated absorption varies significantly with redshift: higher-redshift systems are primarily found in the QSO region, whereas lower-redshift systems are more concentrated in the spiral galaxy region.

The color difference between $W1[3.4\ \mu\text{m}]$ and $W2[4.6\ \mu\text{m}]$, with a value of 0.8, is commonly utilized as a basic mid-infrared color criterion to identify AGN candidates (Stern et al. 2012). Figure 37 illustrates the difference in WISE magnitudes between the W1 and W2 bands plotted against the HI column density. It reveals no apparent correlation between the W1-W2 magnitudes and HI column density in associated systems. However, for the foreground sources in the intervening systems, a potential trend suggests that HI column density diminishes as W1-W2 magnitudes increase. Notably, all identified foreground sources exhibit W1-W2 magnitudes less than 0.8, suggesting that these sources are likely galaxies with minimal or no AGN activity. Figure 37 illustrates that most lower-redshift associ-

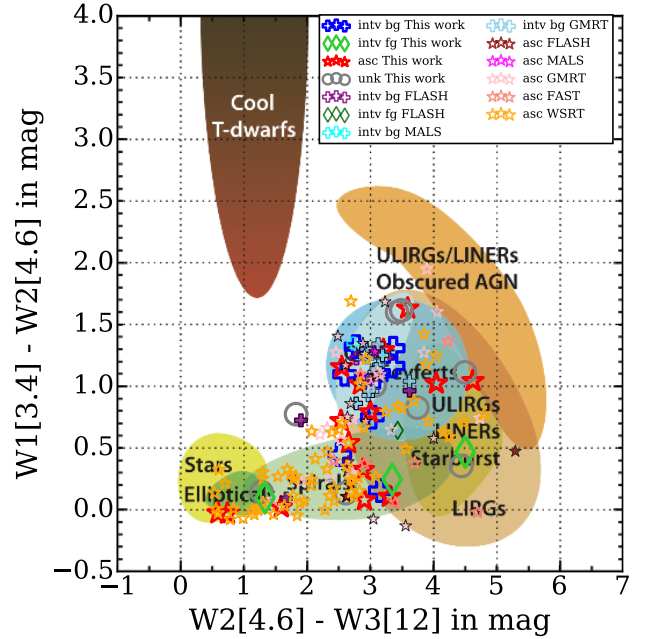


Figure 36. The WISE color-color diagram showing the locations of interesting classes of objects, over-plotted with samples from our work and the literature. Higher- ($z > 0.5$) and lower-redshift ($z \leq 0.5$) samples are represented by filled points and open points, respectively.

ated absorption is found at $W1-W2 < 0.8$, implying that at low redshifts, most associated HI absorption likely originates from galaxies with little AGN activity. In contrast, the associated absorption at higher redshifts shows a broader distribution in W1-W2 values, ranging from -0.1 to 1.7, with nearly half of the systems positioned at $W1-W2 > 0.8$, potentially reflecting galaxy evolution. Additionally, Figure 37 highlights that backgrounds of intervening systems are more likely to have $W1-W2 > 0.8$, suggesting they are AGN candidates.

5.3. Spectral Stacking Results

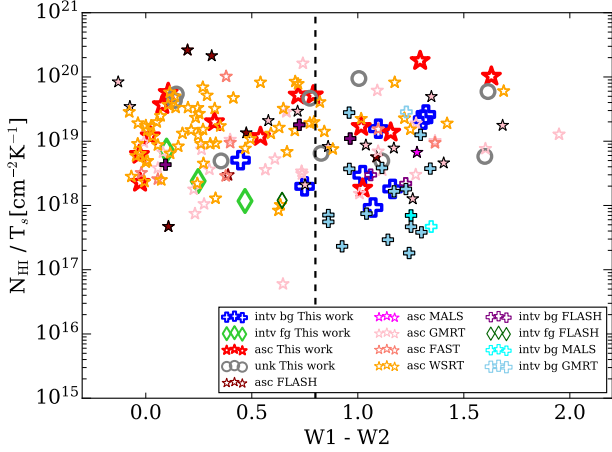


Figure 37. Same as Figure 33, but for WISE magnitude difference between W1 and W2 bands versus the HI column density. The black-dashed line represents a W1-W2 value of 0.8.

Spectral stacking is a technique that combines multiple spectra to enhance weak signals and effectively replicates the overall spectral characteristics (Hu et al. 2019, 2020, 2021). In this section, we examine HI properties of both associated and intervening HI absorption systems. This is achieved by stacking HI absorption spectra from, for the first time, a blind catalog of HI absorbers that was compiled without bias.

The stacking technique used in this paper is similar to that described in Hu et al. (2019). Flux density spectra were converted to optical depth spectra using Eq. (2). We introduce a weight factor that equals the inverse of completeness. The weight of i th HI absorption system is expressed as:

$$w_i = 1/C(W_i, SN_i, \nu_i), \quad (3)$$

where $C(W_i, SN_i, \nu_i)$ refers to the completeness for a HI absorbers with FWHM of W_i , S/N of SN_i and at the frequency of ν_i . The completeness was estimated by adding mock absorption lines to real CRAFTS and FASHI spectra and calculating the fraction detected using our search method and selection threshold.

The averaged final stacked spectrum is obtained from:

$$\langle \tau_{\text{HI}}(\nu) \rangle = \frac{\sum_{i=1}^n w_i \tau_{\text{HI},i}}{\sum_{i=1}^n w_i}. \quad (4)$$

The integrated τ of a stack, or $\langle \tau \rangle$, is then defined as integral along the velocity axis over τ spectrum:

$$\tau_{\text{HI}} = \int_{-\Delta v}^{\Delta v} \langle \tau_{\text{HI}}(v) \rangle dv, \quad (5)$$

where Δv is large enough to capture all signals from the stack (we will later use $\Delta v = 200 \text{ km s}^{-1}$). The

integrated N_{HI} of a stack ($\langle N_{\text{HI}} \rangle$) is then calculated by $1.82 \times 10^{18} T_s \langle \tau \rangle$. The errors for measurements were estimated through jackknife resampling.

The HI absorption used for stacking consists of 33 systems except for NVSS J112832+583346 (emission and absorption are indistinguishable), including 14 associated systems, 10 intervening systems, and 9 unknown-type systems. Stacking optical depth spectra from our sample results in strong detections. The stacked spectra are shown in Figure 38. The mean peak optical path, mean velocity-integrated optical path $\langle \tau \rangle$, mean FWHM and mean HI column density $\langle N_{\text{HI}} \rangle$ are measured to be 0.47 ± 0.10 , 0.30 ± 0.07 and 0.38 ± 0.06 ; $27.19 \pm 8.71 \text{ km s}^{-1}$, $4.36 \pm 1.46 \text{ km s}^{-1}$ and $19.89 \pm 4.83 \text{ km s}^{-1}$; $42.61 \pm 15.62 \text{ km s}^{-1}$, $9.33 \pm 2.08 \text{ km s}^{-1}$ and $34.58 \pm 12.34 \text{ km s}^{-1}$; 0.49 ± 0.16 , 0.08 ± 0.03 and $0.36 \pm 0.08 T_s \times 10^{20} \text{ cm}^{-2} \text{ K}^{-1}$, for associated, intervening and all HI absorption samples.

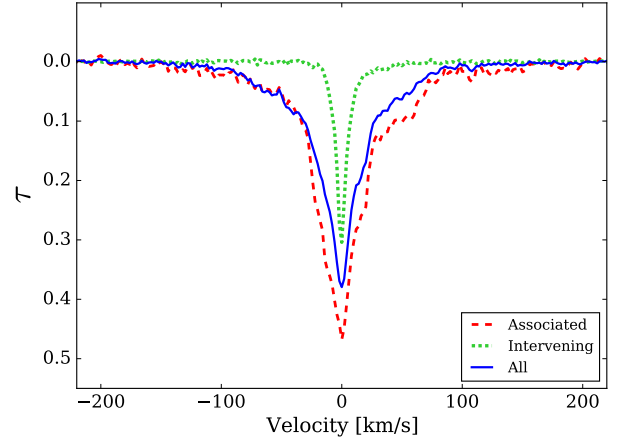


Figure 38. Stack of HI absorption spectra of the associated, intervening, and all HI absorption samples detected in this work.

6. DISCUSSIONS

6.1. Comoving Absorption Path

The absorption path length defines the moving interval of the survey that is sensitive to intervening absorbers. We estimate total comoving absorption path length (ΔX) for the data (CRAFTS and FASHI) used here (1050-1150 MHz and 1250-1450 MHz), adopting the method described in Allison et al. (2015, 2020); Allison (2021) and Paper I.

Assuming the covering factor $c_f = 1$, velocity FWHM $\Delta v_{50} = 30 \text{ km s}^{-1}$ (the mean velocity width for all intervening 21-cm absorbers detected (Curran et al. 2016; Allison et al. 2016)), and a detection threshold of 5.5σ ,

we show the comoving absorption path length for our data as a function of HI column density in Figure 39. We present results for $T_s/c_f = 100$ and 1000 K, which are the typical spin temperature of the cold (CNM) and the warm neutral medium (WNM) respectively (Murray et al. 2018). Under the assumption of $T_s/c_f = 100$ K, the total comoving absorption path length spanned by our data is $\Delta X^{\text{inv}} = 4.72 \times 10^4$ ($\Delta z^{\text{inv}} = 3.74 \times 10^4$) and $\Delta X^{\text{asc}} = 2.04 \times 10^2$ ($\Delta z^{\text{asc}} = 1.48 \times 10^2$). The comoving absorption paths sensitive to the DLAs ($N_{\text{HI}} \geq 2 \times 10^{20} \text{ cm}^{-2}$) are $\Delta X^{\text{inv}} = 4.07 \times 10^4$ ($\Delta z^{\text{inv}} = 3.19 \times 10^4$) for the intervening absorption and $\Delta X^{\text{asc}} = 1.81 \times 10^2$ ($\Delta z^{\text{asc}} = 1.31 \times 10^2$) for the associated absorption, respectively.

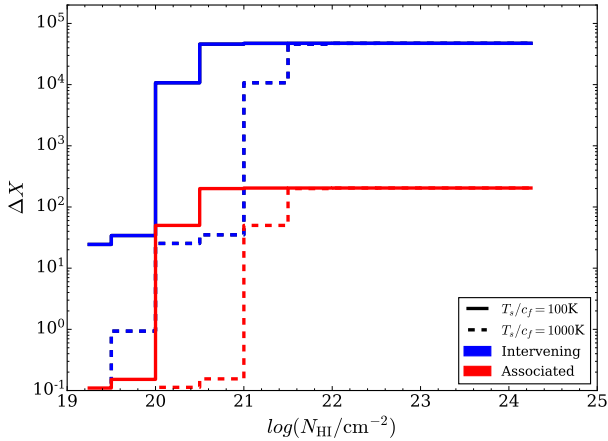


Figure 39. The comoving absorption path length (ΔX) spanned by our data as a function of HI column density sensitivity. The results for spin temperature to source covering fraction ratios of 100 K and 1000 K are shown as blue and red lines, respectively.

6.2. Detection Rate

Our survey is an unbiased blind survey, and it is informative to compare the detection fractions in our sample with those reported in other studies from the literature. The integrated optical depth of the weakest associated and intervening HI absorptions detected in our sample is approximately 1 km s^{-1} and 0.5 km s^{-1} , respectively. To ensure a fair comparison with previous surveys conducted at different redshifts, we base the detection rate estimates on observations where the 3σ upper limits for the velocity-integrated optical depth are $\leq 1 \text{ km s}^{-1}$ and $\leq 0.5 \text{ km s}^{-1}$ for associated and intervening HI absorption, respectively, in both our survey and other surveys. The 3σ upper limits to the velocity integrated optical depth is estimated as $\int \tau dv = -\ln(1 - 3\sigma_{\text{rms}}/S_{\text{cont}}) \times \Delta v$, where S_{cont} represents the

continuum flux density of the targeted radio sources, σ_{rms} is the root mean square(RMS) per noise velocity channel Δv , Δv is the velocity channel resolution, which is selected to be 100 km s^{-1} for associated HI absorption. For cases where the literature reports RMS noise values for different velocity resolutions, the RMS noise is adjusted by dividing by a factor of $\sqrt{100/\Delta v_{\text{rms}}}$, where Δv_{rms} is the velocity channel width corresponding to the reported RMS noise. In the case of intervening systems, we adopt a velocity resolution Δv_{intv} of 30 km s^{-1} and apply a 3σ upper limit for the velocity-integrated optical depth of $\leq 0.5 \text{ km s}^{-1}$. To ensure completeness in our search, we correct the total number of detections by a completeness factor: $N_{\text{total}}^{\text{asc}} = \sum_i^{N^{\text{asc}}} 1/C_i$ and $N_{\text{total}}^{\text{intv}} = \sum_i^{N^{\text{intv}}} 1/C_i$, where N^{asc} and N^{intv} represent the total number of detected HI 21-cm associated and intervening absorptions, respectively.

The detection rates from our survey, along with those from the literature for associated(open points) and intervening(filled points) HI absorption, are shown in Figure 40. If we focus on background sources with a flux density $\geq 40 \text{ mJy}$ at the HI absorption frequency, the detection rate for associated HI absorption in our study is $2.11 \pm 0.55\%$ at $z \sim 0.045$, and for intervening HI absorption, it is $3.02 \pm 1.23\%$ at $z \sim 0.247$. When we limit the analysis to sources with flux density $\geq 400 \text{ mJy}$ at the HI absorption frequency, the detection rates rise to $3.79 \pm 0.46\%$ for associated HI absorption at $z \sim 0.045$ and $5.04 \pm 0.85\%$ for intervening HI absorption at $z \sim 0.186$. While the detection rate for intervening HI absorption is similar to that of associated HI absorption, fewer surveys have targeted intervening systems. This disparity exists because associated HI absorption at low redshift is generally easier to detect, as discussed in Section 5.1.2. However, with the advent of more powerful telescopes like the SKA, its precursors and pathfinders(MALS and FLASH), and the FAST core array(Jiang et al. 2024), we anticipate the detection of more intervening systems in the near future.

Compared to other surveys, our survey shows a lower detection rate for both associated and intervening HI 21-cm absorption. This is primarily because ours is a blind survey, whereas the others specifically target sources with additional information (such as precise redshift data) or particular types of sources (like compact steep spectrum sources or MgII absorbers).

6.3. Statistic Completeness

In this study, we examine characteristics of associated and intervening HI 21-cm absorption using extensive statistical analysis. It is important to acknowledge that the outcomes are significantly influenced by sample

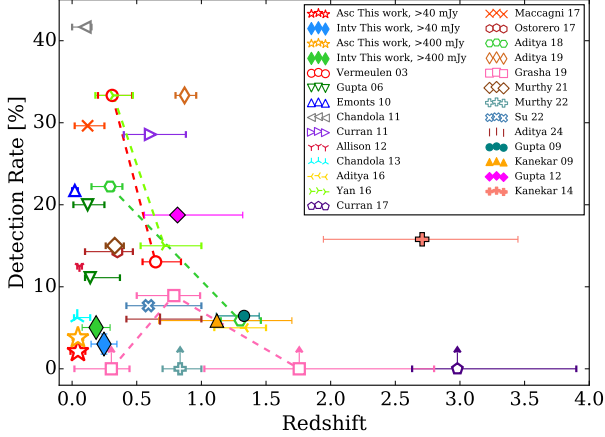


Figure 40. The detection rate of HI 21-cm absorbers from this study and previous literature across different redshift intervals. Only the intervening and associated HI 21-cm absorptions with integrated optical depth limits exceeding 0.5 km s^{-1} and 1 km s^{-1} , respectively, are considered here. Detection rates from the same survey at various redshifts are linked with dashed lines. The detection rates for associated and intervening systems are indicated by open and filled points, respectively. The references for the literature are: Vermeulen et al. (2003); Gupta et al. (2006); Emonts et al. (2010); Chandola et al. (2011, 2013); Curran et al. (2011, 2017); Allison et al. (2012); Aditya et al. (2016, 2024); Yan et al. (2016); Maccagni et al. (2017); Ostorero et al. (2017); Aditya & Kanekar (2018b); Aditya (2019); Grasha et al. (2019); Murthy et al. (2021, 2022); Su et al. (2022); Kanekar et al. (2009, 2014); Gupta et al. (2009, 2012)

completeness. To assess our sample’s completeness, we introduced mock absorption into actual data and conducted the search process again. We identified that the most significant factor affecting completeness was the bandpass fluctuations, primarily due to standing waves. In the FAST data, these standing waves exhibit a frequency width of approximately 1 MHz (equivalent to about 200 km s^{-1} at the redshift of 0), posing a challenge to detect HI absorption features with an FWHM of around 200 km s^{-1} . Nonetheless, the average velocity width for the intervening HI 21-cm absorption is recorded at 30 km s^{-1} , and the FWHM for most associated HI 21-cm absorption remains below 200 km s^{-1} (Geréb et al. 2015). The HI absorption features with an FWHM of around 200 km s^{-1} should be faint absorption systems without peak narrow components. Typical absorption profiles, even with high-speed outflows will keep the FWHM lower than 200 km s^{-1} because these features are shallow, and more visible at the W20 (the width of the spectral line measured at 20% of the peak intensity) level. Given that our analysis has been adjusted for completeness, the findings of this work can

still faithfully reflect the characteristics of the HI 21-cm absorption with FWHM less than 200 km s^{-1} .

Li et al. (2023) introduced a data processing pipeline for the FAST HI intensity mapping drift-scan survey, employing a low-pass filter to mitigate noise and diminish the presence of standing waves. Their calibration approach effectively corrects both the temporal and bandpass gain variations over the 4-hour drift-scan sessions. More recently, Jing et al. (2024) unveiled Hi-FAST, a comprehensive calibration and imaging pipeline specifically designed for FAST HI data, which includes a method for standing wave elimination based on FFT. We plan to incorporate the standing wave removal technique in our future data processing efforts, which is expected to expand our catalog and enhance statistical analyses across a broader parameter space.

7. SUMMARY

In this paper, we present a purely blind search for extragalactic HI 21-cm absorption lines in drift-scan data from FAST. We have examined 1325.6 hours of data from the CRAFTS and FASHI surveys, which covered 6072.0 deg^2 of the sky, with a total of 84533 radio sources with a flux density greater than 12 mJy were searched for HI absorber. The data of both linear polarization of all 19 beams were processed. All data in the frequency range of 1.05 GHz to 1.45 GHz were searched. Assuming an HI spin temperature to source covering fraction ratio of $T_s/c_f = 100 \text{ K}$, the total comoving absorption path length spanned by our data and sensitive to the Damped Lyman α Absorbers (DLAs; $N_{\text{HI}} \geq 2 \times 10^{20} \text{ cm}^{-2}$) is $\Delta X^{\text{inv}} = 4.07 \times 10^4$ ($\Delta z^{\text{inv}} = 3.19 \times 10^4$) for intervening absorption. For associated absorption, the corresponding value is $\Delta X^{\text{asc}} = 1.81 \times 10^2$ ($\Delta z^{\text{asc}} = 1.31 \times 10^2$). A matched-filtering approach was used to detect HI absorption profiles.

We successfully detected 14 known HI absorbers and 20 new HI 21-cm absorbers, comprising 15 associated systems, 10 intervening systems, and 9 systems with undetermined classifications. We fit the HI profiles with multi-components Gaussian functions, and calculate the redshift, width, flux density, optical depth, and HI column densities for each source. In our study, the detection rate for associated HI absorption with integrated optical depth limits above 1 km s^{-1} is $2.11 \pm 0.55\%$ at $z \sim 0.045$, and for intervening HI absorption with integrated optical depth limits above 0.5 km s^{-1} , it is $3.02 \pm 1.23\%$ at $z \sim 0.247$. Statistical analysis reveals the following results:

- Most associated HI absorption systems are observed at lower redshifts ($z < 0.2$) while intervening systems appear more often at higher redshifts ($z > 0.2$).

Table 1. Some basic physical parameters of the associated/background radio sources. The positional values are obtained from NED, while the flux density is measured at the redshifted HI 21-cm frequency in our calibrated spectra.

Radio Source	Source Type	Ra(J2000)	Dec(J2000)	cz (km s ⁻¹)	S _ν (mJy)
NVSS J004219+570836 [◇]	QSO	00h 42m 19.45s	+57d 08m 36.59s	342063.24	1660.31 ± 27.94
4C +56.02 [⊗]	Radio Source	01h 10m 57.55s	+56d 32m 16.98s	-	2104.72 ± 34.93
NVSS J011322+251852 [◇]	Radio Galaxy	01h 13m 22.69s	+25d 18m 53.26s	208355.79	58.69 ± 1.42
4C +31.04 [*]	Double Radio System	01h 19m 35.00s	+32d 10m 50.05s	18047.51 ± 59.96	2898.42 ± 47.85
4C +26.07 [⊗]	Radio Source	02h 05m 37.34s	+26d 50m 02.70s	107625.49 ± 43409.95	320.72 ± 5.37
3C 84 [*]	Radio Galaxy	03h 19m 48.16s	+41d 30m 42.11s	5264 ± 11 km/s	18736.21 ± 310.17
NVSS J033529+195621 [⊗]	Radio Source	03h 35m 29.43s	+19d 56m 21.3s	-	65.89 ± 1.25
NVSS J040845+001306 [*]	Radio Source	04h 08m 45.29s	+00d 13m 07.35s	8945 ± 35	48.79 ± 2.42
NVSS J055437+271126 [⊗]	Radio Galaxy	05h 54m 37.30s	+27d 11m 25.9s	27855.52	39.77 ± 0.82
NVSS J073755+264652 [*]	Radio Galaxy	07h 37m 55.34s	+26d 46m 52.57s	71685.18 ± 17.69	71.91 ± 2.34
4C -06.18 [⊗]	Radio Source	07h 44m 21.66s	-06d 29m 35.93s	-	12326.00 ± 203.46
NVSS J080101-075121 [⊗]	Radio Source	08h 01m 01.01s	-07d 51m 21.80s	41371.36 ± 12111.62	118.8 ± 3.6
NVSS J085521+575143 [◇]	Radio Source	08h 55m 21.36s	+57d 51m 44.09s	132598.20	751.55 ± 119.75
NVSS J092351+281527 [◇]	QSO	09h 23m 51.52s	+28d 15m 25.02s	223196 ± 35	596.19 ± 9.88
NVSS J093150+254034 [◇]	Radio Galaxy	09h 31m 50.56s	+25d 40m 34.61s	243552 ± 35	178.59 ± 5.08
NVSS J094208+135152 [◇]	Radio Source	09h 42m 08.40s	+13d 51m 52.2s	-	1414.06 ± 22.40
NVSS J095058+375758 [*]	Radio Galaxy	09h 50m 58.72s	+37d 57m 58.40s	12149 ± 4	79.78 ± 2.31
NVSS J095812+112643 [⊗]	Radio Galaxy	09h 58m 12.35s	+11d 26m 42.62s	94134.83 ± 23024.06	423.66 ± 6.82
NVSS J100755+405519 [⊗]	Radio Source	10h 07m 55.69s	+40d 55m 18.50s	57260.36 ± 44369.28	81.99±3.44
NVSS J104941+133255 [◇]	QSO	10h 49m 41.10s	+13d 32m 55.68s	828592 ± 75	145.90 ± 5.16
NVSS J112832+583346 [*]	Radio Galaxy	11h 28m 32.30s	+58d 33m 43.0s	3121 ± 3	675.48±11.53
NVSS J115948+582020 [◇]	Radio Galaxy	11h 59m 48.77s	+58d 20m 20.28s	188419.59	1651.43 ± 28.61
NVSS J134035+444817 [*]	Radio Galaxy	13h 40m 35.20s	+44d 48m 17.40s	19619 ± 2	41.04±2.69
4C +57.23 [◇]	Radio Source	13h 54m 00.12s	+56d 50m 04.74s	62956	767.88 ± 13.04
NVSS J141314-031227 [*]	Radio Galaxy	14h 13m 14.89s	-03d 12m 27.28s	1824 ± 3	353.07 ± 6.52
NVSS J141558+132024 [◇]	QSO	14h 15m 58.82s	+13d 20m 23.71s	73962 ± 3	1359.21 ± 22.75
NVSS J160332+171158 [*]	Radio Galaxy	16h 03m 32.08s	+17d 11m 55.31s	10198 ± 2	501.78 ± 8.52
NVSS J162549+402921 [*]	Radio Source	16h 25m 50.03s	+40d 29m 18.84s	8747 ± 3	84.42 ± 3.50
NVSS J225900+274356 [*]	Radio Source	22h 59m 00.31s	+27d 43m 56.70s	32977 ± 6895	589.74 ± 9.62

* Associated HI absorption type.
 ◇ Intervening HI absorption type.
 ⊗ Unknown HI absorption type.

- In our sample the associated systems tend to be hosted by red ($g - r > 0.7$) galaxies at lower redshifts, whereas the galaxies hosting intervening HI absorption are typically found at higher redshifts and are of a bluer ($g - r \leq 0.7$) type.
- It has been demonstrated that associated HI 21-cm absorption connected to compact radio sources display higher N_{HI} compared to those tied to extended radio sources.
- Only a small fraction of intervening absorption systems currently have identified foreground sources. With the upcoming capabilities of the SKA and the FAST core array, we expect to detect more of these intervening systems.
- Most (three out of four WISE-identified foregrounds) foreground absorption systems appear in the spiral galaxy region of the WISE color-color diagram, while the backgrounds cluster around the QSO region. Host galaxies of associated absorptions spread widely, with most in the spiral region, though high-redshift hosts ($z > 0.5$) tend to occupy the QSO region.
- For foreground sources within the intervening systems in our sample, there appears to be a potential trend indicating that HI column density decreases as W1-W2 magnitudes increase. All identified foreground sources display W1-W2 magnitudes below 0.8, implying these sources are likely galaxies with little or no AGN activity. In contrast, backgrounds of intervening systems are more likely to have W1-W2 magnitudes above 0.8, suggesting they are AGN candidates. For

Table 2. WISE magnitudes for the WISE counterparts of background radio sources (WISE magnitudes for foreground sources of intervening systems, if available, is presented in the context). The identifications of counterparts for NVSS J094208+135152, and 4C+57.23 are unclear due to the proximity between foreground and background objects.

Radio Source	WISE Counterpart	W1	W2	W3	W4	WISE color-color classification
NVSS J004219+570836	WISEA J004219.53+570836.0	14.577	13.413	10.047	7.579	QSOs & Seyferts
4C+56.02	WISEA J011057.55+563216.8	14.795	14.021	12.190	8.956	-
NVSS J011322+251852	WISEA J011322.69+251853.2	14.355	13.047	9.679	7.269	QSOs
4C+31.04	WISEA J011935.00+321050.2	11.641	11.620	10.024	7.578	Spirals
4C+26.07	WISEA J020537.42+265003.8	14.942	13.343	9.912	7.476	QSOs
3C 84	WISEA J031948.16+413042.3	9.136	8.113	4.062	1.150	Seyferts & Starburst
NVSS J033529+195621	WISEA J033529.35+195620.7	14.360	12.746	9.248	6.276	QSOs
NVSS J040845+001306	WISEA J040845.31+001308.0	11.511	11.433	8.520	6.698	Spirals
NVSS J055437+271126	WISEA J055437.35+271126.3	12.257	12.113	10.830	8.318	Ellipticals/Spirals
NVSS J073755+264652	WISEA J073755.33+264652.9	14.356	14.032	11.138	8.279	Spirals
4C-06.18	WISEA J074421.66-062935.7	15.440	14.327	9.821	6.232	LIRG
NVSS J080101-075121	WISEA J080101.19-075123.0	15.097	14.962	12.345	8.642	Spirals
NVSS J085521+575143	WISEA J085521.34+575144.5	15.126	14.971	11.808	8.772	Spirals/LIRGs
NVSS J092351+281527	WISEA J092351.52+281525.1	14.117	13.045	9.946	7.721	QSOs
NVSS J093150+254034	WISEA J093150.56+254034.6	15.339	14.590	11.552	8.263	Seyferts
NVSS J094208+135152	-	-	-	-	-	-
NVSS J095058+375758	WISEA J095058.73+375758.3	11.933	11.143	8.138	5.728	Seyferts
NVSS J095812+112643	WISEA J095812.38+112643.3	16.130	15.775	11.327	8.551	ULIRGs/LINERs/Starburst
NVSS J100755+405519	WISEA J100755.72+405517.7	15.927	14.922	11.848	8.360	QSOs
NVSS J104941+133255	WISEA J104941.17+133251.9	15.281	14.834	12.309	8.586	Spirals
NVSS J112832+583346	WISEA J112833.59+583346.5	9.342	8.299	3.667	0.726	ULIRGs/LINERs
NVSS J115948+582020	WISEA J115948.76+582020.2	16.207	15.110	12.511	9.314	Seyferts
NVSS J134035+444817	WISEA J134035.20+444817.3	11.066	10.050	7.202	4.728	QSOs
4C+57.23	-	-	-	-	-	-
NVSS J141314-031227	WISEA J141314.88-031227.5	7.399	6.244	3.692	1.068	Seyferts/QSOs
NVSS J141558+132024	WISEA J141558.82+132023.7	12.160	10.839	8.058	5.755	QSOs
NVSS J160332+171158	WISEA J160332.08+171155.3	10.939	10.966	10.372	8.476	Ellipticals
NVSS J162549+402921	WISEA J162549.96+402919.4	10.764	10.794	10.049	8.646	Ellipticals
NVSS J225900+274356	WISEA J225900.29+274356.9	13.148	12.429	9.887	7.551	Seyferts/QSOs

associated absorption, most low-redshift systems show W1-W2 values below 0.8, while associated absorption at higher redshifts ($z > 0.5$) exhibits a wider range of W1-W2 values.

- Through spectral stacking, mean peak optical path, mean velocity-integrated optical path $\langle \tau \rangle$, mean FWHM and mean HI column density $\langle N_{\text{HI}} \rangle$ are measured to be 0.47 and 0.30; 27.19 km s^{-1} and 4.36 km s^{-1} ; 42.61 km s^{-1} and 9.33 km s^{-1} ; 0.49 and 0.08 $T_s \times 10^{20} \text{cm}^{-2} \text{K}^{-1}$, for associated and intervening samples, respectively.

ACKNOWLEDGEMENTS

This work made use of the data from FAST (Five-hundred-meter Aperture Spherical radio Tele-

scope)(<https://cstr.cn/31116.02.FAST>). FAST is a Chinese national mega-science facility, operated by National Astronomical Observatories, Chinese Academy of Sciences. This work is supported by the National SKA Program of China (Nos. 2022SKA0110100 and 2022SKA0110101), the NSFC International (Regional) Cooperation and Exchange Project (No. 12361141814), and NSFC grants (Nos. 11973047, 12203061, 12303004). WH acknowledges support from the South African Radio Astronomy Observatory and National Research Foundation (Grant No. 84156). The authors thank Snežana Stanimirović, James R. Allison, and Renzhi Su for helpful discussion.

DATA AVAILABILITY

Table 3. SDSS magnitudes for the SDSS counterparts of background sources (SDSS magnitudes for foreground sources of intervening systems, if available, is presented in the context). Several background sources lack SDSS counterparts because they fall outside the coverage area of SDSS.

Radio Source	SDSS Counterpart	u	g	r	i	z
NVSS J004219+570836	-	-	-	-	-	-
4C +56.02	-	-	-	-	-	-
NVSS J011322+251852	SDSS J011322.69+251853.2	20.650	19.921	19.126	18.586	18.242
4C +31.04	SDSS J011934.99+321050.0	17.266	15.077	14.056	13.552	13.191
4C +26.07	SDSS J020537.32+265001.5	22.497	21.744	20.689	20.066	20.411
3C 84	SDSS J031948.15+413042.1	13.492	12.030	11.314	10.981	10.720
NVSS J033529+195621	-	-	-	-	-	-
NVSS J040845+001306	SDSS J040845.31+001307.2	17.278	15.288	14.234	13.644	13.133
NVSS J055437+271126	-	-	-	-	-	-
NVSS J073755+264652	SDSS J073755.33+264652.6	21.214	19.746	18.477	17.902	17.394
4C -06.18	-	-	-	-	-	-
NVSS J080101-075121	SDSS J080101.20-075123.3	24.094	20.079	19.107	18.560	18.200
NVSS J085521+575143	SDSS J085521.37+575144.1	22.514	21.667	20.140	19.547	19.198
NVSS J092351+281527	SDSS J092351.52+281525.1	19.698	19.198	19.091	19.021	18.808
NVSS J093150+254034	-	-	-	-	-	-
NVSS J094208+135152	SDSS J094208.05+135154.9	20.724	19.471	18.889	18.614	18.536
NVSS J095058+375758	SDSS J095058.69+375758.8	17.847	16.194	15.342	14.852	14.450
NVSS J095812+112643	SDSS J095812.32+112642.5	24.484	22.480	21.018	20.518	19.505
NVSS J100755+405519	SDSS J100755.68+405518.5	24.644	22.095	21.401	20.895	21.325
NVSS J104941+133255	SDSS J104941.09+133255.6	19.841	18.827	18.713	18.741	18.569
NVSS J112832+583346	SDSS J112833.41+583346.2	14.333	13.368	12.559	12.326	11.979
NVSS J115948+582020	SDSS J115948.76+582020.0	22.127	21.688	20.957	20.674	20.773
NVSS J134035+444817	SDSS J134035.20+444817.3	17.999	16.776	16.164	15.739	15.457
4C +57.23	SDSS J135400.09+565004.9	24.108	23.173	22.603	21.732	22.675
NVSS J141314-031227	SDSS J141314.87-031227.3	14.644	12.898	12.019	11.385	11.268
NVSS J141558+132024	SDSS J141558.81+132023.7	22.064	20.518	19.049	18.496	18.056
NVSS J160332+171158	SDSS J160332.08+171155.3	16.276	14.374	13.432	12.981	12.716
NVSS J162549+402921	SDSS J162549.96+402919.3	15.697	13.800	12.974	12.536	12.204
NVSS J225900+274356	SDSS J225900.30+274356.7	19.479	17.964	17.154	16.642	16.390

The radio data analyzed in this work can be accessed by sending a request to the FAST Data Centre or the corresponding authors of this paper.

APPENDIX

A. GAUSSIAN MODEL SELECTION

When fitting models, adding more parameters can increase the maximum likelihood, but this often leads to overfitting. To address this, the Bayesian Information Criterion (BIC; Schwarz 1978; Kass & Raftery 1995) is used in statistics for model selection among a finite set of models. BIC introduces a penalty term for the number of parameters to prevent overfitting. Its main objective is to identify the best model by balancing the goodness of fit with model complexity. In general, models with lower BIC values are preferred. The BIC is formally defined as:

$$\text{BIC} = k \ln(n) - 2 \ln(\hat{L}), \quad (\text{A1})$$

where k is the number of parameters estimated by the model, n is the number of data points, and \hat{L} is the maximum value of the likelihood function for the model. For each HI absorption, we fitted the spectra from follow-up observations using models with varying numbers of Gaussian functions and calculated the BIC for each. The model with the lowest BIC was chosen for the final HI absorption profile fitting and the estimation of physical parameters.

Table 4. Some basic physical parameters for known absorption are shown in this paper. The associated, intervening, and unknown types are labeled with star, diamond, and cross, respectively.

Radio Source	Comp	cz_{peak} (km s^{-1})	FWHM (km s^{-1})	$S_{\text{HI, peak}}$ (mJy)	$\int S_{\text{HI}} dv$ (mJy km s^{-1})	$\tau_{\text{peak}} \times 10^2$	$\int \tau dv$ (km s^{-1})	N_{HI}/T_s ($10^{18} \text{cm}^{-2} \text{K}^{-1}$)
4C +56.02 [⊙]	1	79415.66±0.18	11.28±0.45	-40.13±1.47	-481.66±26.40	1.92±0.06	0.23±0.01	0.42±0.02
	2	79375.09±0.47	38.01±0.88	-98.48±2.05	-3984.32±128.49	4.79±0.06	1.93±0.05	3.50±0.10
	3	79314.52±0.35	29.45±2.19	-581.73±31.25	-18235.41±1680.70	32.35±1.95	9.67±0.91	17.59±1.66
	4	79297.70±0.08	15.90±0.32	-443.39±31.77	-7505.57±562.49	23.66±1.86	3.87±0.31	7.04±0.56
	5	79311.73±0.78	58.67±1.49	-184.12±24.28	-11497.78±1547.26	9.15±1.25	5.64±0.78	10.27±1.42
	6	79332.25±0.14	15.79±0.47	-237.52±24.62	-3992.35±431.67	11.97±1.30	1.98±0.22	3.60±0.40
	Total	79301.40±0.41	46.32±1.43	-885.85±29.18	-45697.09±845.04	54.63±2.08	25.82±0.21	46.99±0.39
4C +31.04*	1	17823.24±1.81	49.68±4.55	-16.78±2.42	-887.36±151.90	0.58±0.08	0.31±0.05	0.56±0.10
	2	17904.56±1.50	54.78±7.01	-20.08±5.03	-1170.81±329.73	0.70±0.17	0.40±0.11	0.74±0.21
	3	17946.14±2.95	142.00±2.76	-101.32±2.77	-15314.23±549.60	3.56±0.08	5.35±0.17	9.73±0.32
	4	18020.67±0.90	27.36±2.79	-9.17±0.79	-267.24±35.87	0.32±0.03	0.09±0.01	0.17±0.02
	5	18131.48±0.47	6.73±1.12	-8.57±1.16	-61.40±13.22	0.30±0.04	0.02±0.00	0.04±0.01
	6	18150.80±0.26	14.79± 0.43	-48.14±3.05	-758.07±53.77	1.67±0.10	0.26±0.02	0.48±0.03
	7	18154.00±0.11	6.04±0.37	-44.90±3.16	-288.57±27.17	1.56±0.11	0.10±0.01	0.18±0.02
Total	17926.39±2.61	151.94±2.97	-108.96±3.00	-18747.67±377.37	3.83±0.09	6.55±0.08	11.93±0.15	
3C 84 HV5 [⊙]	1	8118.94±0.55	23.52±0.78	-381.80±26.41	-9560.18±739.80	2.06±0.14	0.51±0.04	0.94±0.07
	2	8120.26±0.08	3.82±0.24	-467.78±27.02	-1901.94±164.65	2.53±0.14	0.10±0.01	0.19±0.02
	3	8113.26±0.02	5.56±0.06	-2604.56±54.06	-15424.63±395.06	14.97±0.20	0.87±0.02	1.58±0.03
	4	8105.77±0.09	4.25±0.25	-468.40±24.89	-2118.82±170.27	2.53±0.13	0.11±0.01	0.21±0.02
	Total	8113.30±0.20	6.13±0.32	-2929.92±56.54	-29005.56±562.80	17.01±0.19	1.62±0.02	2.94±0.03
3C 84*	1	5159.24±29.14	271.67±56.13	-32.67±3.03	-9445.91±2154.60	0.17±0.02	0.50±0.11	0.91±0.21
	2	5417.57±15.13	208.67±26.59	-49.58±4.91	-11012.97±1801.26	0.26±0.03	0.59±0.10	1.07±0.17
	Total	5408.06±21.60	435.66±40.23	-52.49±4.08	-20458.88±624.17	0.28±0.02	1.09±0.03	1.98±0.05
4C -06.18 [⊙]	1	95443.11±1.45	50.67±3.90	-39.16±2.60	-2112.01±214.61	0.32±0.02	0.17±0.02	0.31±0.03
	2	95566.33±0.45	24.10±1.44	-77.85±4.01	-1997.22±157.71	0.63±0.03	0.16±0.01	0.30±0.02
	3	95587.42±4.97	154.69±14.36	-76.15±2.81	-12539.51±1252.49	0.62±0.02	1.02±0.10	1.86±0.18
	4	95684.00±2.69	29.69±11.03	-22.76±10.35	-719.28±422.43	0.18±0.08	0.06±0.03	0.11±0.06
	5	95727.47±0.24	16.85±0.79	-143.78±6.50	-2578.97±168.04	1.17±0.05	0.21±0.01	0.38±0.02
	6	95721.51±3.08	85.96±3.63	-151.93±10.83	-13902.37±1152.62	1.24±0.09	1.13±0.09	2.06±0.17
Total	95727.15±3.30	48.93±7.43	-301.76±7.91	-33849.36±530.66	24.79±0.05	2.76±0.01	5.02±0.01	
NVSS J085521+575143 [⊙]	1	7737.48±0.04	3.40±0.15	-152.67±9.75	-553.36±44.37	25.34±1.79	0.88±0.07	1.61±0.13
	2	7739.17±0.50	6.84±0.55	-36.67±8.82	-266.84±67.92	5.53±1.36	0.40±0.10	0.73±0.19
	Total	7737.56±0.19	3.80±0.28	-183.91±9.68	-820.21±22.36	31.42±1.86	1.33±0.03	2.41±0.06
NVSS J112832+583346*	1	3093.46±4.05	65.26±9.31	-24.26±2.14	-1685.23±285.07	-	-	-
	2	3185.46±3.76	74.43±9.08	-27.79±2.04	-2201.76±316.76	-	-	-
	Total	3185.02±3.89	158.32±9.18	-27.89±2.09	-3886.99±103.87	-	-	-
NVSS J134035+444817*	1	19615.98±0.02	8.08±0.04	-26.92±0.43	-231.62±15.89	106.71±12.10	7.81±0.82	14.22±1.49
	2	19601.39±0.01	2.18±0.03	-14.99±0.31	-34.75±2.48	45.46±3.72	0.98±0.09	1.79±0.16
	Total	19615.98±0.02	8.09±0.04	-26.92±0.44	-266.37±18.20	106.71±12.10	8.80±0.37	16.01±0.66
4C +57.23 [⊙]	1	28554.18±0.13	13.34±0.30	-112.87±2.68	-1603.41±67.99	15.90±0.32	2.21±0.09	4.02±0.16
	2	28586.70±0.56	29.81±1.44	-38.34±1.51	-1216.82±82.54	5.12±0.19	1.61±0.11	2.94±0.20
	Total	28554.27±0.31	13.69±0.30	-114.30±2.50	-2820.23±87.46	16.12±0.28	3.83±0.10	6.96±0.19
NVSS J141314-031227*	1	1793.54±0.92	36.34±4.63	-20.39±3.83	-788.65±179.96	5.85±1.13	2.25±0.52	4.09±0.94
	2	1835.52±8.77	88.28±12.65	-14.86±1.23	-1396.91±233.01	4.23±0.35	3.95±0.66	7.20±1.20
	3	1750.99±1.92	13.34±5.18	-5.16±1.72	-73.19±37.49	1.45±0.49	0.21±0.11	0.37±0.19
	4	1967.18±0.69	8.50±1.66	-12.06±1.88	-109.09±27.39	3.42±0.54	0.31±0.08	0.56±0.14
	5	1988.74±0.85	21.19±2.21	-15.80±1.22	-356.36±46.93	4.51±0.35	1.01±0.13	1.84±0.24
Total	1796.39±4.96	70.81±8.32	-28.66±2.05	-2724.20±72.15	8.33±0.61	7.78±0.13	14.16±0.24	
NVSS J141558+132024 [⊙]	1	73947.99±0.15	8.43±0.36	-131.97±7.15	-1184.52±81.60	10.21±0.56	0.90±0.06	1.64±0.11
	2	73959.82±0.08	14.00±0.43	-366.30±24.56	-5459.84±402.28	31.40±2.41	4.47±0.35	8.13±0.64
	3	73961.54±0.32	25.42±0.68	-261.89±24.03	-7087.14±677.90	21.40±2.16	5.61±0.57	10.21±1.04
	4	73992.74±2.18	101.72±3.44	-23.72±1.09	-2568.21±146.61	1.76±0.08	1.90±0.10	3.46±0.19
Total	73960.11±0.52	21.20±1.01	-643.71±24.47	-16299.72±254.45	64.17±3.13	14.31±0.01	26.05±0.02	
NVSS J160332+171158*	1	10205.76±0.85	6.17±2.77	-5.63±1.91	-36.97±20.80	1.13±0.39	0.07±0.04	0.13±0.08
	2	10223.57±1.08	28.93±1.89	-18.00±1.16	-554.32±51.22	3.65±0.23	1.12±0.10	2.04±0.19
	3	10219.03±1.00	4.77±2.95	-4.26±2.02	-21.64±16.88	0.85±0.41	0.04±0.03	0.08±0.06
	Total	10219.49±1.07	31.60±1.98	-21.19±1.25	-612.93±11.69	4.31±0.25	1.24±0.02	2.25±0.03

Table 5. Same as Table 4, but for new detected HI absorption shown in this paper.

Radio Source	Comp	cz_{peak} (km s^{-1})	FWHM (km s^{-1})	$S_{\text{HI, peak}}$ (mJy)	$\int S_{\text{HI}} dv$ (mJy km s^{-1})	$\tau_{\text{peak}} \times 10^2$	$\int \tau dv$ (km s^{-1})	N_{HI} / T_s ($10^{18} \text{cm}^{-2} \text{K}^{-1}$)
NVSS J004219+570836 $^\circ$	1	79032.90 \pm 0.02	3.12 \pm 0.10	-205.40 \pm 12.02	-682.79 \pm 45.31	13.21 \pm 0.79	0.43 \pm 0.03	0.78 \pm 0.05
	2	79035.75 \pm 0.29	6.32 \pm 0.42	-97.46 \pm 6.76	-655.78 \pm 63.53	6.05 \pm 0.42	0.40 \pm 0.04	0.73 \pm 0.07
	3	79039.81 \pm 1.04	17.03 \pm 1.29	-14.83 \pm 2.45	-268.81 \pm 48.97	0.90 \pm 0.15	0.16 \pm 0.03	0.30 \pm 0.05
	Total	79033.10 \pm 0.30	4.24 \pm 0.43	-272.44 \pm 9.07	-1607.39 \pm 27.56	17.92 \pm 0.58	1.02 \pm 0.01	1.85 \pm 0.01
NVSS J011322+251852 $^\circ$	1	76385.99 \pm 0.21	13.53 \pm 0.78	-13.41 \pm 0.96	-193.19 \pm 17.82	25.95 \pm 2.14	3.60 \pm 0.35	6.55 \pm 0.64
	2	76391.39 \pm 0.71	34.84 \pm 1.68	-10.26 \pm 0.96	-380.63 \pm 40.21	19.22 \pm 2.00	6.93 \pm 0.78	12.61 \pm 1.42
	3	76424.11 \pm 0.51	7.69 \pm 1.32	-3.23 \pm 0.45	-26.47 \pm 5.85	5.67 \pm 0.81	0.46 \pm 0.10	0.84 \pm 0.19
	Total	76386.52 \pm 0.54	19.39 \pm 1.37	-23.08 \pm 0.99	-600.29 \pm 9.92	49.96 \pm 2.84	11.73 \pm 0.11	21.36 \pm 0.21
4C +26.07 $^\circ$	1	75179.93 \pm 0.83	24.42 \pm 3.37	-9.90 \pm 2.28	-257.45 \pm 69.07	3.14 \pm 0.73	0.81 \pm 0.22	1.48 \pm 0.40
	2	75198.50 \pm 0.36	12.38 \pm 0.83	-11.89 \pm 0.88	-156.68 \pm 15.72	3.78 \pm 0.28	0.50 \pm 0.05	0.90 \pm 0.09
	3	75180.84 \pm 0.83	51.24 \pm 3.68	-10.81 \pm 2.34	-589.36 \pm 134.82	3.43 \pm 0.75	1.86 \pm 0.43	3.39 \pm 0.78
	Total	75196.81 \pm 0.75	41.88 \pm 3.16	-22.17 \pm 2.12	-1003.49 \pm 17.59	7.16 \pm 0.70	3.21 \pm 0.02	5.84 \pm 0.04
NVSS J033529+195621 $^\circ$	1	87558.50 \pm 10.44	82.80 \pm 9.40	-12.84 \pm 2.85	-1131.77 \pm 282.60	21.68 \pm 5.36	18.50 \pm 4.91	33.68 \pm 8.94
	2	87611.86 \pm 8.98	73.22 \pm 7.36	-10.53 \pm 3.80	-820.99 \pm 307.78	17.42 \pm 6.86	13.23 \pm 5.26	24.08 \pm 9.57
	Total	87583.92 \pm 0.73	112.37 \pm 1.21	-16.92 \pm 0.33	-1952.77 \pm 42.44	29.68 \pm 0.56	32.97 \pm 0.40	60.01 \pm 0.74
NVSS J040845+001306*	1	8938.21 \pm 1.41	56.91 \pm 3.70	-12.51 \pm 0.95	-758.19 \pm 77.19	29.64 \pm 3.08	17.18 \pm 2.06	31.28 \pm 3.74
	2	8928.80 \pm 0.29	4.46 \pm 0.75	-16.28 \pm 2.29	-77.24 \pm 16.97	40.61 \pm 7.43	1.81 \pm 0.44	3.30 \pm 0.79
	3	8937.80 \pm 0.87	5.21 \pm 2.28	-5.91 \pm 2.15	-32.79 \pm 18.68	12.91 \pm 5.05	0.70 \pm 0.41	1.28 \pm 0.75
	Total	8928.84 \pm 1.29	16.08 \pm 3.39	-27.89 \pm 1.18	-868.22 \pm 21.12	84.77 \pm 8.44	20.65 \pm 0.25	37.59 \pm 0.46
NVSS J055437+271126 $^\circ$	1	14282.00 \pm 1.48	48.46 \pm 2.28	-7.20 \pm 0.38	-371.21 \pm 26.20	19.96 \pm 1.14	10.00 \pm 0.73	18.20 \pm 1.33
	2	14340.71 \pm 1.41	63.72 \pm 4.38	-9.34 \pm 0.21	-633.51 \pm 45.93	26.77 \pm 0.65	17.45 \pm 1.27	31.76 \pm 2.31
	3	14378.90 \pm 0.97	21.13 \pm 3.60	-2.68 \pm 0.46	-60.30 \pm 14.57	6.98 \pm 1.24	1.55 \pm 0.38	2.83 \pm 0.69
	Total	14339.09 \pm 1.41	121.95 \pm 3.60	-9.48 \pm 0.28	-1065.02 \pm 17.54	27.22 \pm 0.90	29.66 \pm 0.21	53.98 \pm 0.39
NVSS J073755+264652*	1	71621.72 \pm 0.14	13.92 \pm 0.34	-39.50 \pm 1.03	-585.12 \pm 23.57	79.70 \pm 4.17	10.47 \pm 0.41	19.06 \pm 0.75
NVSS J080101-075121 $^\circ$	1	27414.93 \pm 2.68	47.72 \pm 5.52	-34.91 \pm 2.15	-1773.50 \pm 232.98	34.73 \pm 3.47	16.76 \pm 2.61	30.50 \pm 4.74
	2	27442.87 \pm 0.71	14.52 \pm 2.41	-38.38 \pm 5.56	-593.23 \pm 130.65	38.94 \pm 7.40	5.68 \pm 1.41	10.34 \pm 2.56
	Total	27441.92 \pm 2.19	50.79 \pm 4.74	-52.31 \pm 3.05	-2366.73 \pm 43.17	57.90 \pm 6.37	23.34 \pm 0.95	42.48 \pm 1.73
NVSS J092351+281527 $^\circ$	1	99217.81 \pm 0.81	13.33 \pm 1.69	-19.65 \pm 1.62	-279.02 \pm 53.09	33.55 \pm 0.28	0.47 \pm 0.09	0.86 \pm 0.16
	2	99210.55 \pm 0.30	3.04 \pm 0.88	-16.62 \pm 4.02	-53.73 \pm 21.15	2.83 \pm 0.69	0.09 \pm 0.04	0.17 \pm 0.06
	Total	99210.75 \pm 0.73	14.23 \pm 1.56	-25.46 \pm 2.02	-332.75 \pm 38.66	43.67 \pm 3.49	0.57 \pm 0.06	1.03 \pm 0.11
NVSS J093150+254034 $^\circ$	1	80339.26 \pm 0.07	2.51 \pm 0.16	-60.43 \pm 3.39	-161.71 \pm 5.46	41.30 \pm 0.03	1.04 \pm 0.17	1.89 \pm 0.32
NVSS J094208+135152 $^\circ$	1	39901.98 \pm 1.34	20.74 \pm 2.82	-16.93 \pm 4.29	-373.70 \pm 107.63	1.20 \pm 0.31	0.27 \pm 0.08	0.48 \pm 0.14
	2	39903.49 \pm 0.31	5.87 \pm 0.72	-63.76 \pm 5.00	-398.34 \pm 58.13	4.61 \pm 0.36	0.29 \pm 0.04	0.52 \pm 0.08
	3	39909.17 \pm 0.83	4.77 \pm 1.51	-20.71 \pm 4.99	-105.11 \pm 41.78	1.48 \pm 0.36	0.07 \pm 0.03	0.14 \pm 0.05
	Total	39903.51 \pm 0.81	8.60 \pm 1.71	-80.85 \pm 4.82	-877.16 \pm 14.22	5.89 \pm 0.35	0.63 \pm 0.02	1.15 \pm 0.03
NVSS J095058+375758*	1	12202.08 \pm 0.23	35.23 \pm 0.54	-46.07 \pm 0.94	-1727.84 \pm 30.54	86.14 \pm 0.04	28.38 \pm 0.37	51.65 \pm 0.67
NVSS J095812+112643 $^\circ$	1	95828.71 \pm 0.05	7.69 \pm 0.21	-61.20 \pm 2.26	-500.94 \pm 23.38	23.14 \pm 0.63	1.25 \pm 0.06	2.27 \pm 0.10
	2	95827.53 \pm 0.22	20.26 \pm 0.78	-26.57 \pm 2.16	-572.89 \pm 51.57	15.60 \pm 0.57	1.38 \pm 0.12	2.52 \pm 0.23
	Total	95828.64 \pm 0.14	9.54 \pm 0.52	-87.53 \pm 2.49	-1073.82 \pm 17.73	6.48 \pm 0.53	2.71 \pm 0.01	4.94 \pm 0.01
NVSS J100755+405519 $^\circ$	1	67051.73 \pm 0.81	11.56 \pm 1.93	-9.97 \pm 1.43	-122.67 \pm 27.03	12.97 \pm 2.04	1.57 \pm 0.36	2.85 \pm 0.65
	2	67079.17 \pm 0.34	6.50 \pm 1.02	-21.57 \pm 2.92	-149.13 \pm 30.94	30.53 \pm 4.97	2.02 \pm 0.45	3.67 \pm 0.81
	3	67088.58 \pm 1.56	22.18 \pm 2.53	-24.61 \pm 1.52	-581.01 \pm 75.42	35.68 \pm 3.00	7.99 \pm 1.11	14.55 \pm 2.03
	4	67105.29 \pm 1.45	9.34 \pm 2.31	-32.31 \pm 10.31	-321.04 \pm 129.62	50.10 \pm 20.86	4.62 \pm 2.13	8.41 \pm 3.87
	5	67116.37 \pm 0.79	11.59 \pm 4.45	-60.95 \pm 4.58	-751.91 \pm 294.11	136.05 \pm 23.77	13.64 \pm 5.57	24.83 \pm 10.14
	6	67126.05 \pm 0.84	8.54 \pm 1.40	-58.59 \pm 15.48	-532.55 \pm 165.50	125.38 \pm 66.67	9.42 \pm 4.66	17.15 \pm 8.49
	Total	67137.91 \pm 0.43	10.01 \pm 0.92	-35.58 \pm 1.68	-379.02 \pm 39.34	56.91 \pm 4.42	5.57 \pm 0.65	10.14 \pm 1.18
NVSS J104941+133255 $^\circ$	1	73958.31 \pm 0.11	5.45 \pm 0.25	-57.07 \pm 2.43	-331.45 \pm 24.54	49.53 \pm 3.27	2.67 \pm 0.25	4.86 \pm 0.46
NVSS J115948+582020 $^\circ$	1	71474.54 \pm 0.10	3.47 \pm 0.37	-149.76 \pm 27.20	-553.11 \pm 116.71	9.51 \pm 1.81	0.35 \pm 0.07	0.63 \pm 0.14
	2	71475.90 \pm 0.21	12.51 \pm 0.17	-603.46 \pm 51.30	-8034.81 \pm 691.79	45.48 \pm 4.83	5.66 \pm 0.57	10.30 \pm 1.03
	3	71478.65 \pm 0.33	7.84 \pm 0.83	-302.32 \pm 56.23	-2521.73 \pm 539.16	20.22 \pm 4.16	1.64 \pm 0.37	2.98 \pm 0.67
	Total	71475.70 \pm 0.23	10.95 \pm 0.33	-917.04 \pm 52.53	-11109.65 \pm 175.56	81.04 \pm 6.94	8.69 \pm 0.01	15.81 \pm 0.02
NVSS J162549+402921*	1	8776.56 \pm 0.75	17.51 \pm 1.76	-12.43 \pm 1.10	-231.80 \pm 35.15	15.93 \pm 1.66	2.90 \pm 0.78	5.28 \pm 1.41
NVSS J225900+274356*	1	42738.30 \pm 1.96	113.76 \pm 4.43	-55.02 \pm 5.83	-6662.34 \pm 754.05	9.79 \pm 1.08	11.69 \pm 1.35	21.28 \pm 2.46
	2	42754.27 \pm 1.21	61.95 \pm 4.29	-39.57 \pm 5.96	-2609.05 \pm 433.04	6.94 \pm 1.08	4.53 \pm 0.76	8.25 \pm 1.39
	3	42850.82 \pm 5.61	336.03 \pm 7.55	-20.34 \pm 0.70	-7276.34 \pm 303.37	3.51 \pm 0.11	12.49 \pm 0.49	22.73 \pm 0.89
	Total	42750.67 \pm 3.44	100.47 \pm 5.78	-108.34 \pm 3.91	-16547.73 \pm 285.55	20.30 \pm 0.74	29.58 \pm 0.19	53.83 \pm 0.35

Figure 41 presents the fitting results for the HI absorption of the HVS in the 3C 84 system using three, four, and five Gaussian models. The fit with three Gaussian functions produces residual spectra with significant fluctuations, indicating that this model is insufficient to accurately capture the HI absorption profile. Although the five-Gaussian model results in residual spectra with minimal fluctuations, the fifth Gaussian component (represented by the magenta dashed line) appears unnecessary, with no clear physical interpretation, suggesting overfitting. On the other hand, the four-Gaussian model also yields a flat residual spectrum with minimal fluctuations and achieves the lowest BIC value, making it the optimal model we adopted for the HI absorption in the HVS from the 3C 84 system.

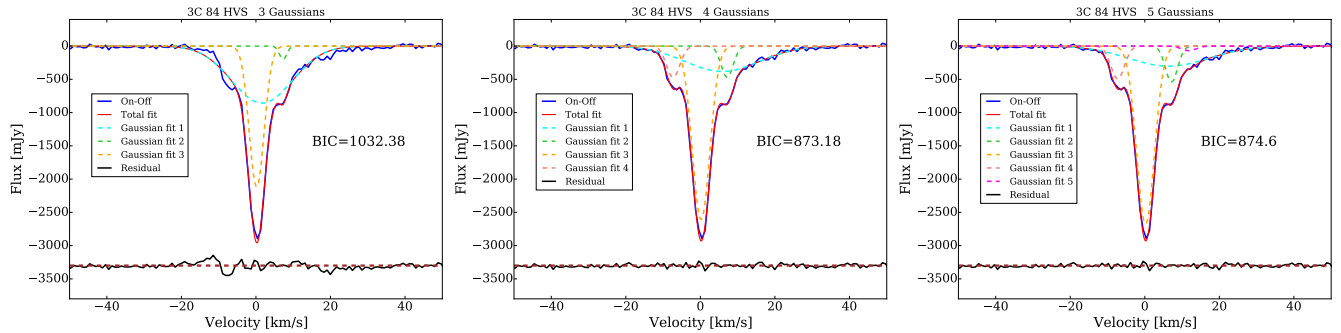


Figure 41. The fitting results for the HI absorption of the HVS in the 3C 84 system using three, four, and five Gaussian models are displayed in the left, center, and right panels, respectively. The BIC values for each model are also provided in the corresponding panels.

REFERENCES

- Aditya, J. N. H. S. 2019, *MNRAS*, 482, 5597, doi: [10.1093/mnras/sty3062](https://doi.org/10.1093/mnras/sty3062)
- Aditya, J. N. H. S., Jorgenson, R., Joshi, V., et al. 2021, *MNRAS*, 500, 998, doi: [10.1093/mnras/staa3306](https://doi.org/10.1093/mnras/staa3306)
- Aditya, J. N. H. S., & Kanekar, N. 2018a, *MNRAS*, 473, 59, doi: [10.1093/mnras/stx2325](https://doi.org/10.1093/mnras/stx2325)
- . 2018b, *MNRAS*, 481, 1578, doi: [10.1093/mnras/sty2184](https://doi.org/10.1093/mnras/sty2184)
- Aditya, J. N. H. S., Kanekar, N., & Kurapati, S. 2016, *MNRAS*, 455, 4000, doi: [10.1093/mnras/stv2563](https://doi.org/10.1093/mnras/stv2563)
- Aditya, J. N. H. S., Yoon, H., Allison, J. R., et al. 2024, *MNRAS*, 527, 8511, doi: [10.1093/mnras/stad3722](https://doi.org/10.1093/mnras/stad3722)
- Allison, J. R. 2021, *MNRAS*, 503, 985, doi: [10.1093/mnras/stab518](https://doi.org/10.1093/mnras/stab518)
- Allison, J. R., Zwaan, M. A., Duchesne, S. W., & Curran, S. J. 2016, *MNRAS*, 462, 1341, doi: [10.1093/mnras/stw1722](https://doi.org/10.1093/mnras/stw1722)
- Allison, J. R., Curran, S. J., Emonts, B. H. C., et al. 2012, *MNRAS*, 423, 2601, doi: [10.1111/j.1365-2966.2012.21062.x](https://doi.org/10.1111/j.1365-2966.2012.21062.x)
- Allison, J. R., Sadler, E. M., Moss, V. A., et al. 2015, *MNRAS*, 453, 1249, doi: [10.1093/mnras/stv1532](https://doi.org/10.1093/mnras/stv1532)
- Allison, J. R., Sadler, E. M., Bellstedt, S., et al. 2020, *MNRAS*, 494, 3627, doi: [10.1093/mnras/staa949](https://doi.org/10.1093/mnras/staa949)
- Allison, J. R., Sadler, E. M., Amaral, A. D., et al. 2022, *PASA*, 39, e010, doi: [10.1017/pasa.2022.3](https://doi.org/10.1017/pasa.2022.3)
- Augarde, R., & Lequeux, J. 1985, *A&A*, 147, 273
- Baan, W. A., & Haschick, A. 1990, *ApJ*, 364, 65, doi: [10.1086/169385](https://doi.org/10.1086/169385)
- Becker, R. H., White, R. L., & Helfand, D. J. 1995, *ApJ*, 450, 559, doi: [10.1086/176166](https://doi.org/10.1086/176166)
- Beichman, C. A., Neugebauer, G., Soifer, B. T., et al. 1981, *Nature*, 293, 711, doi: [10.1038/293711a0](https://doi.org/10.1038/293711a0)
- Biggs, A. D., Zwaan, M. A., Hatziminaoglou, E., Péroux, C., & Liske, J. 2016, *MNRAS*, 462, 2819, doi: [10.1093/mnras/stw1786](https://doi.org/10.1093/mnras/stw1786)
- Bordoloi, R., O’Meara, J. M., Sharon, K., et al. 2022, *Nature*, 606, 59, doi: [10.1038/s41586-022-04616-1](https://doi.org/10.1038/s41586-022-04616-1)
- Bregman, J. N., Lebofsky, M. J., Aller, M. F., et al. 1981, *Nature*, 293, 714, doi: [10.1038/293714a0](https://doi.org/10.1038/293714a0)
- Carilli, C. L., Perlman, E. S., & Stocke, J. T. 1992, *ApJL*, 400, L13, doi: [10.1086/186637](https://doi.org/10.1086/186637)
- Casoli, F., Combes, F., Augarde, R., Figon, P., & Martin, J. M. 1989, *A&A*, 224, 31
- Caultet, A., Woodgate, B. E., Brown, L. W., et al. 1992, *ApJ*, 388, 301, doi: [10.1086/171153](https://doi.org/10.1086/171153)
- Chambers, K. C., Magnier, E. A., Metcalfe, N., et al. 2016, *arXiv e-prints*, arXiv:1612.05560, doi: [10.48550/arXiv.1612.05560](https://doi.org/10.48550/arXiv.1612.05560)
- Chandola, Y., Gupta, N., & Saikia, D. J. 2013, *MNRAS*, 429, 2380, doi: [10.1093/mnras/sts499](https://doi.org/10.1093/mnras/sts499)
- Chandola, Y., & Saikia, D. J. 2017, *MNRAS*, 465, 997, doi: [10.1093/mnras/stw2705](https://doi.org/10.1093/mnras/stw2705)

- Chandola, Y., Saikia, D. J., & Li, D. 2020, *MNRAS*, 494, 5161, doi: [10.1093/mnras/staa1029](https://doi.org/10.1093/mnras/staa1029)
- Chandola, Y., Saikia, D. J., Ma, Y.-Z., et al. 2024, *ApJ*, 973, 48, doi: [10.3847/1538-4357/ad5d5c](https://doi.org/10.3847/1538-4357/ad5d5c)
- Chandola, Y., Sirothia, S. K., & Saikia, D. J. 2011, *MNRAS*, 418, 1787, doi: [10.1111/j.1365-2966.2011.19607.x](https://doi.org/10.1111/j.1365-2966.2011.19607.x)
- Cohen, A. S., Lane, W. M., Cotton, W. D., et al. 2007, *AJ*, 134, 1245, doi: [10.1086/520719](https://doi.org/10.1086/520719)
- Combes, F., Gupta, N., Muller, S., et al. 2023, *A&A*, 671, A43, doi: [10.1051/0004-6361/202245482](https://doi.org/10.1051/0004-6361/202245482)
- Curran, S. J. 2017, *A&A*, 606, A56, doi: [10.1051/0004-6361/201731666](https://doi.org/10.1051/0004-6361/201731666)
- Curran, S. J., Duchesne, S. W., Divoli, A., & Allison, J. R. 2016, *MNRAS*, 462, 4197, doi: [10.1093/mnras/stw1938](https://doi.org/10.1093/mnras/stw1938)
- Curran, S. J., Hunstead, R. W., Johnston, H. M., et al. 2017, *MNRAS*, 470, 4600, doi: [10.1093/mnras/stx1572](https://doi.org/10.1093/mnras/stx1572)
- Curran, S. J., Whiting, M. T., Murphy, M. T., et al. 2011, *MNRAS*, 413, 1165, doi: [10.1111/j.1365-2966.2011.18209.x](https://doi.org/10.1111/j.1365-2966.2011.18209.x)
- Darling, J. 2012, *ApJL*, 761, L26, doi: [10.1088/2041-8205/761/2/L26](https://doi.org/10.1088/2041-8205/761/2/L26)
- de Vries, N., Snellen, I. A. G., Schilizzi, R. T., Mack, K. H., & Kaiser, C. R. 2009, *A&A*, 498, 641, doi: [10.1051/0004-6361/200811145](https://doi.org/10.1051/0004-6361/200811145)
- De Young, D. S., Roberts, M. S., & Saslaw, W. C. 1973, *ApJ*, 185, 809, doi: [10.1086/152456](https://doi.org/10.1086/152456)
- Deka, P. P., Gupta, N., Chen, H. W., et al. 2024a, *A&A*, 687, A50, doi: [10.1051/0004-6361/202348464](https://doi.org/10.1051/0004-6361/202348464)
- Deka, P. P., Gupta, N., Jagannathan, P., et al. 2024b, *ApJS*, 270, 33, doi: [10.3847/1538-4365/acf7b9](https://doi.org/10.3847/1538-4365/acf7b9)
- Dickey, J. M. 1986, *ApJ*, 300, 190, doi: [10.1086/163793](https://doi.org/10.1086/163793)
- . 1997, *AJ*, 113, 1939, doi: [10.1086/118408](https://doi.org/10.1086/118408)
- Dickey, J. M., & Benson, J. M. 1982, *AJ*, 87, 278, doi: [10.1086/113103](https://doi.org/10.1086/113103)
- Dickey, J. M., McClure-Griffiths, N., Gibson, S. J., et al. 2013, *PASA*, 30, e003, doi: [10.1017/pasa.2012.003](https://doi.org/10.1017/pasa.2012.003)
- Dickey, J. M., Dempsey, J. M., Pingel, N. M., et al. 2022, *ApJ*, 926, 186, doi: [10.3847/1538-4357/ac3a89](https://doi.org/10.3847/1538-4357/ac3a89)
- Douglas, J. N., Bash, F. N., Bozyan, F. A., Torrence, G. W., & Wolfe, C. 1996, *AJ*, 111, 1945, doi: [10.1086/117932](https://doi.org/10.1086/117932)
- Dunning, A., Bowen, M., Castillo, S., et al. 2017, in 2017 XXXIInd General Assembly and Scientific Symposium of the International Union of Radio Science (URSI GASS), 1–4, doi: [10.23919/URSIGASS.2017.8105012](https://doi.org/10.23919/URSIGASS.2017.8105012)
- Dutta, R. 2019, *Journal of Astrophysics and Astronomy*, 40, 41, doi: [10.1007/s12036-019-9610-5](https://doi.org/10.1007/s12036-019-9610-5)
- Dutta, R., Srianand, R., & Gupta, N. 2018, *MNRAS*, 480, 947, doi: [10.1093/mnras/sty1872](https://doi.org/10.1093/mnras/sty1872)
- Emonts, B. H. C., Morganti, R., Struve, C., et al. 2010, *MNRAS*, 406, 987, doi: [10.1111/j.1365-2966.2010.16706.x](https://doi.org/10.1111/j.1365-2966.2010.16706.x)
- Fischer, J., Simon, M., Benson, J., & Solomon, P. M. 1983, *ApJL*, 273, L27, doi: [10.1086/184123](https://doi.org/10.1086/184123)
- Fritz, J., Franceschini, A., & Hatziminaoglou, E. 2006, *MNRAS*, 366, 767, doi: [10.1111/j.1365-2966.2006.09866.x](https://doi.org/10.1111/j.1365-2966.2006.09866.x)
- Gallimore, J. F., Baum, S. A., O’Dea, C. P., Pedlar, A., & Brinks, E. 1999, *ApJ*, 524, 684, doi: [10.1086/307853](https://doi.org/10.1086/307853)
- Gehrz, R. D., Sramek, R. A., & Weedman, D. W. 1983, *ApJ*, 267, 551, doi: [10.1086/160892](https://doi.org/10.1086/160892)
- Geréb, K., Maccagni, F. M., Morganti, R., & Oosterloo, T. A. 2015, *A&A*, 575, A44, doi: [10.1051/0004-6361/201424655](https://doi.org/10.1051/0004-6361/201424655)
- Geréb, K., Morganti, R., & Oosterloo, T. A. 2014, *A&A*, 569, A35, doi: [10.1051/0004-6361/201423999](https://doi.org/10.1051/0004-6361/201423999)
- Giovannini, G., Cotton, W. D., Feretti, L., Lara, L., & Venturi, T. 2001, *ApJ*, 552, 508, doi: [10.1086/320581](https://doi.org/10.1086/320581)
- Gioiretti, M., Giovannini, G., Taylor, G. B., et al. 2003, *A&A*, 399, 889, doi: [10.1051/0004-6361:20021821](https://doi.org/10.1051/0004-6361:20021821)
- Grasha, K., Darling, J., Bolatto, A., Leroy, A. K., & Stocke, J. T. 2019, *ApJS*, 245, 3, doi: [10.3847/1538-4365/ab4906](https://doi.org/10.3847/1538-4365/ab4906)
- Gupta, N., Salter, C. J., Saikia, D. J., Ghosh, T., & Jeyakumar, S. 2006, *MNRAS*, 373, 972, doi: [10.1111/j.1365-2966.2006.11064.x](https://doi.org/10.1111/j.1365-2966.2006.11064.x)
- Gupta, N., Srianand, R., Petitjean, P., et al. 2012, *A&A*, 544, A21, doi: [10.1051/0004-6361/201219159](https://doi.org/10.1051/0004-6361/201219159)
- Gupta, N., Srianand, R., Petitjean, P., Noterdaeme, P., & Saikia, D. J. 2009, *MNRAS*, 398, 201, doi: [10.1111/j.1365-2966.2009.14933.x](https://doi.org/10.1111/j.1365-2966.2009.14933.x)
- Gupta, N., Jagannathan, P., Srianand, R., et al. 2021, *ApJ*, 907, 11, doi: [10.3847/1538-4357/abcb85](https://doi.org/10.3847/1538-4357/abcb85)
- Healey, S. E., Romani, R. W., Taylor, G. B., et al. 2007, *ApJS*, 171, 61, doi: [10.1086/513742](https://doi.org/10.1086/513742)
- Heiles, C., & Troland, T. H. 2003, *ApJ*, 586, 1067, doi: [10.1086/367828](https://doi.org/10.1086/367828)
- Helmboldt, J. F., Taylor, G. B., Tremblay, S., et al. 2007, *ApJ*, 658, 203, doi: [10.1086/511005](https://doi.org/10.1086/511005)
- Helou, G., Madore, B. F., Schmitz, M., et al. 1991, *The NASA/IPAC extragalactic database.*, ed. M. A. Albrecht & D. Egret, Vol. 171, 89–106, doi: [10.1007/978-94-011-3250-3_10](https://doi.org/10.1007/978-94-011-3250-3_10)
- Hu, W., Catinella, B., Cortese, L., et al. 2020, *MNRAS*, 493, 1587, doi: [10.1093/mnras/staa257](https://doi.org/10.1093/mnras/staa257)
- Hu, W., Cortese, L., Staveley-Smith, L., et al. 2021, *MNRAS*, 507, 5580, doi: [10.1093/mnras/stab2431](https://doi.org/10.1093/mnras/stab2431)
- Hu, W., Hoppmann, L., Staveley-Smith, L., et al. 2019, *MNRAS*, 489, 1619, doi: [10.1093/mnras/stz2038](https://doi.org/10.1093/mnras/stz2038)
- Hu, W., Wang, Y., Li, Y., et al. 2023, *A&A*, 675, A40, doi: [10.1051/0004-6361/202245549](https://doi.org/10.1051/0004-6361/202245549)
- Jaffe, W. 1990, *A&A*, 240, 254

- Jiang, P., Tang, N.-Y., Hou, L.-G., et al. 2020, *Research in Astronomy and Astrophysics*, 20, 064, doi: [10.1088/1674-4527/20/5/64](https://doi.org/10.1088/1674-4527/20/5/64)
- Jiang, P., Chen, R., Gan, H., et al. 2024, *Astronomical Techniques and Instruments*, 1, 84, doi: [10.61977/ati2024012](https://doi.org/10.61977/ati2024012)
- Jiao, K., Zhang, J.-C., Zhang, T.-J., et al. 2020, *JCAP*, 2020, 054, doi: [10.1088/1475-7516/2020/01/054](https://doi.org/10.1088/1475-7516/2020/01/054)
- Jing, Y., Wang, J., Xu, C., et al. 2024, *Science China Physics, Mechanics, and Astronomy*, 67, 259514, doi: [10.1007/s11433-023-2333-8](https://doi.org/10.1007/s11433-023-2333-8)
- Kanekar, N., Prochaska, J. X., Ellison, S. L., & Chengalur, J. N. 2009, *MNRAS*, 396, 385, doi: [10.1111/j.1365-2966.2009.14661.x](https://doi.org/10.1111/j.1365-2966.2009.14661.x)
- Kanekar, N., Prochaska, J. X., Smette, A., et al. 2014, *MNRAS*, 438, 2131, doi: [10.1093/mnras/stt2338](https://doi.org/10.1093/mnras/stt2338)
- Kang, J., Lu, C.-Z., Zhang, T.-J., & Zhu, M. 2024, *Research in Astronomy and Astrophysics*, 24, 075002, doi: [10.1088/1674-4527/ad48d1](https://doi.org/10.1088/1674-4527/ad48d1)
- Kass, R. E., & Raftery, A. E. 1995, *Journal of the American Statistical Association*, 90, 773. <http://www.jstor.org/stable/2291091>
- Kloeckner, H. R., Obreschkow, D., Martins, C., et al. 2015, in *Advancing Astrophysics with the Square Kilometre Array (AASKA14)*, 27. <https://arxiv.org/abs/1501.03822>
- Lacy, M., Baum, S. A., Chandler, C. J., et al. 2020, *PASP*, 132, 035001, doi: [10.1088/1538-3873/ab63eb](https://doi.org/10.1088/1538-3873/ab63eb)
- Li, D., Wang, P., Qian, L., et al. 2018, *IEEE Microwave Magazine*, 19, 112, doi: [10.1109/MMM.2018.2802178](https://doi.org/10.1109/MMM.2018.2802178)
- Li, Y., Wang, Y., Deng, F., et al. 2023, *ApJ*, 954, 139, doi: [10.3847/1538-4357/ace896](https://doi.org/10.3847/1538-4357/ace896)
- Lu, C.-Z., Zhang, T., & Zhang, T.-J. 2023, *MNRAS*, 521, 3150, doi: [10.1093/mnras/stad761](https://doi.org/10.1093/mnras/stad761)
- Ma, Z., Xu, H., Zhu, J., et al. 2019, *ApJS*, 240, 34, doi: [10.3847/1538-4365/aaf9a2](https://doi.org/10.3847/1538-4365/aaf9a2)
- Maccagni, F. M., Morganti, R., Oosterloo, T. A., Geréb, K., & Maddox, N. 2017, *A&A*, 604, A43, doi: [10.1051/0004-6361/201730563](https://doi.org/10.1051/0004-6361/201730563)
- Mahony, E. K., Allison, J. R., Sadler, E. M., et al. 2022, *MNRAS*, 509, 1690, doi: [10.1093/mnras/stab3041](https://doi.org/10.1093/mnras/stab3041)
- Maina, E. K., Mohapatra, A., Józsa, G. I. G., et al. 2022, *MNRAS*, 516, 2050, doi: [10.1093/mnras/stac1752](https://doi.org/10.1093/mnras/stac1752)
- Martin, D. C., Fanson, J., Schiminovich, D., et al. 2005, *ApJL*, 619, L1, doi: [10.1086/426387](https://doi.org/10.1086/426387)
- McCarthy, P. J., Miley, G. K., de Koff, S., et al. 1997, *ApJS*, 112, 415, doi: [10.1086/313035](https://doi.org/10.1086/313035)
- McHardy, I. M., Abraham, R. G., Crawford, C. S., et al. 1991, *MNRAS*, 249, 742, doi: [10.1093/mnras/249.4.742](https://doi.org/10.1093/mnras/249.4.742)
- Momjian, E., Romney, J. D., & Troland, T. H. 2002, *The Astrophysical Journal*, 566, 195, doi: [10.1086/337993](https://doi.org/10.1086/337993)
- Morganti, R., & Oosterloo, T. 2018, *A&A Rv*, 26, 4, doi: [10.1007/s00159-018-0109-x](https://doi.org/10.1007/s00159-018-0109-x)
- Morganti, R., Murthy, S., Oosterloo, T., et al. 2023, *A&A*, 678, A42, doi: [10.1051/0004-6361/202347117](https://doi.org/10.1051/0004-6361/202347117)
- Murray, C. E., Stanimirović, S., Goss, W. M., et al. 2018, *ApJS*, 238, 14, doi: [10.3847/1538-4365/aad81a](https://doi.org/10.3847/1538-4365/aad81a)
- Murthy, S., Morganti, R., Kanekar, N., & Oosterloo, T. 2022, *A&A*, 659, A185, doi: [10.1051/0004-6361/202142550](https://doi.org/10.1051/0004-6361/202142550)
- Murthy, S., Morganti, R., Oosterloo, T., & Maccagni, F. M. 2021, *A&A*, 654, A94, doi: [10.1051/0004-6361/202141566](https://doi.org/10.1051/0004-6361/202141566)
- Myers, A. D., Palanque-Delabrouille, N., Prakash, A., et al. 2015, *ApJS*, 221, 27, doi: [10.1088/0067-0049/221/2/27](https://doi.org/10.1088/0067-0049/221/2/27)
- Nagar, N. M., Oliva, E., Marconi, A., & Maiolino, R. 2002, *A&A*, 391, L21, doi: [10.1051/0004-6361:20021039](https://doi.org/10.1051/0004-6361:20021039)
- Nair, P. B., & Abraham, R. G. 2010, *ApJS*, 186, 427, doi: [10.1088/0067-0049/186/2/427](https://doi.org/10.1088/0067-0049/186/2/427)
- Nan, R., Li, D., Jin, C., et al. 2011, *International Journal of Modern Physics D*, 20, 989, doi: [10.1142/S0218271811019335](https://doi.org/10.1142/S0218271811019335)
- O'Dea, C. P., Sarazin, C. L., & Owen, F. N. 1987, *ApJ*, 316, 113, doi: [10.1086/165183](https://doi.org/10.1086/165183)
- Oh, K., Koss, M., Markwardt, C. B., et al. 2018, *ApJS*, 235, 4, doi: [10.3847/1538-4365/aaa7fd](https://doi.org/10.3847/1538-4365/aaa7fd)
- Ostorero, L., Morganti, R., Diaferio, A., et al. 2017, *ApJ*, 849, 34, doi: [10.3847/1538-4357/aa8ef6](https://doi.org/10.3847/1538-4357/aa8ef6)
- Perlman, E. S., Carilli, C. L., Stocke, J. T., & Conway, J. 1996, *AJ*, 111, 1839, doi: [10.1086/117922](https://doi.org/10.1086/117922)
- Perlman, E. S., Stocke, J. T., Carilli, C. L., et al. 2002, *AJ*, 124, 2401, doi: [10.1086/344109](https://doi.org/10.1086/344109)
- Perlman, E. S., Stocke, J. T., Conway, J., & Reynolds, C. 2001, *AJ*, 122, 536, doi: [10.1086/321149](https://doi.org/10.1086/321149)
- Rahmani, H., Srianand, R., Gupta, N., et al. 2012, *MNRAS*, 425, 556, doi: [10.1111/j.1365-2966.2012.21503.x](https://doi.org/10.1111/j.1365-2966.2012.21503.x)
- Readhead, A. C. S., Ravi, V., Lioudakis, I., et al. 2021, *ApJ*, 907, 61, doi: [10.3847/1538-4357/abd08c](https://doi.org/10.3847/1538-4357/abd08c)
- Roger, R. S., Caswell, J. L., Murray, J. D., Cole, D. J., & Cooke, D. J. 1978, *MNRAS*, 182, 209, doi: [10.1093/mnras/182.2.209](https://doi.org/10.1093/mnras/182.2.209)
- Rubin, V. C. 1978, *ApJL*, 224, L55, doi: [10.1086/182758](https://doi.org/10.1086/182758)
- Sadler, E. M., Moss, V. A., Allison, J. R., et al. 2020, *MNRAS*, 499, 4293, doi: [10.1093/mnras/staa2390](https://doi.org/10.1093/mnras/staa2390)
- Saintonge, A. 2007, *AJ*, 133, 2087, doi: [10.1086/513515](https://doi.org/10.1086/513515)
- Saraf, M., Wong, O. I., Cortese, L., & Koribalski, B. S. 2023, *MNRAS*, 519, 4128, doi: [10.1093/mnras/stac3695](https://doi.org/10.1093/mnras/stac3695)
- Schwarz, G. 1978, *Annals of Statistics*, 6, 461
- Skrutskie, M. F., Cutri, R. M., Stiening, R., et al. 2006, *AJ*, 131, 1163, doi: [10.1086/498708](https://doi.org/10.1086/498708)

- Srianand, R., Gupta, N., Petitjean, P., et al. 2022, MNRAS, 516, 1339, doi: [10.1093/mnras/stac1877](https://doi.org/10.1093/mnras/stac1877)
- Stern, D., Assef, R. J., Benford, D. J., et al. 2012, ApJ, 753, 30, doi: [10.1088/0004-637X/753/1/30](https://doi.org/10.1088/0004-637X/753/1/30)
- Struve, C., & Conway, J. E. 2012, A&A, 546, A22, doi: [10.1051/0004-6361/201218768](https://doi.org/10.1051/0004-6361/201218768)
- Su, R., Sadler, E. M., Allison, J. R., et al. 2022, MNRAS, 516, 2947, doi: [10.1093/mnras/stac2257](https://doi.org/10.1093/mnras/stac2257)
- Thuan, T. X., & Wadiak, E. J. 1982, ApJ, 252, 125, doi: [10.1086/159539](https://doi.org/10.1086/159539)
- van Gorkom, J. H., Knapp, G. R., Ekers, R. D., et al. 1989, AJ, 97, 708, doi: [10.1086/115016](https://doi.org/10.1086/115016)
- Varenius, E., Costagliola, F., Klöckner, H. R., et al. 2017, A&A, 607, A43, doi: [10.1051/0004-6361/201629819](https://doi.org/10.1051/0004-6361/201629819)
- Vermeulen, R. C., Pihlström, Y. M., Tschager, W., et al. 2003, A&A, 404, 861, doi: [10.1051/0004-6361:20030468](https://doi.org/10.1051/0004-6361:20030468)
- Weedman, D. W. 1972, ApJ, 171, 5, doi: [10.1086/151250](https://doi.org/10.1086/151250)
- Weng, S., Sadler, E. M., Foster, C., et al. 2022, MNRAS, 512, 3638, doi: [10.1093/mnras/stac747](https://doi.org/10.1093/mnras/stac747)
- Wilson, A. S., Penston, M. V., Fosbury, R. A. E., & Boksenberg, A. 1976, MNRAS, 177, 673, doi: [10.1093/mnras/177.3.673](https://doi.org/10.1093/mnras/177.3.673)
- Wolfe, A. M., Gawiser, E., & Prochaska, J. X. 2005, ARA&A, 43, 861, doi: [10.1146/annurev.astro.42.053102.133950](https://doi.org/10.1146/annurev.astro.42.053102.133950)
- Wolfire, M. G., McKee, C. F., Hollenbach, D., & Tielens, A. G. G. M. 2003, ApJ, 587, 278, doi: [10.1086/368016](https://doi.org/10.1086/368016)
- Wright, E. L., Eisenhardt, P. R. M., Mainzer, A. K., et al. 2010, AJ, 140, 1868, doi: [10.1088/0004-6256/140/6/1868](https://doi.org/10.1088/0004-6256/140/6/1868)
- Yan, T., Stocke, J. T., Darling, J., et al. 2016, AJ, 151, 74, doi: [10.3847/0004-6256/151/3/74](https://doi.org/10.3847/0004-6256/151/3/74)
- York, D. G., Adelman, J., Anderson, John E., J., et al. 2000, AJ, 120, 1579, doi: [10.1086/301513](https://doi.org/10.1086/301513)
- Yu, H.-R., Zhang, T.-J., & Pen, U.-L. 2014, PhRvL, 113, 041303, doi: [10.1103/PhysRevLett.113.041303](https://doi.org/10.1103/PhysRevLett.113.041303)
- Yu, Q., Fang, T., Wang, J., & Wu, J. 2023, ApJ, 952, 144, doi: [10.3847/1538-4357/acdb76](https://doi.org/10.3847/1538-4357/acdb76)
- Zhang, B., Zhu, M., Wu, Z.-Z., et al. 2021, MNRAS, 503, 5385, doi: [10.1093/mnras/stab754](https://doi.org/10.1093/mnras/stab754)
- Zhang, C.-P., Zhu, M., Jiang, P., et al. 2024, Science China Physics, Mechanics, and Astronomy, 67, 219511, doi: [10.1007/s11433-023-2219-7](https://doi.org/10.1007/s11433-023-2219-7)
- Zheng, Z., Li, D., Sadler, E. M., Allison, J. R., & Tang, N. 2020, MNRAS, 499, 3085, doi: [10.1093/mnras/staa3033](https://doi.org/10.1093/mnras/staa3033)
- Zovaro, H. R. M., Sharp, R., Nesvadba, N. P. H., et al. 2019, MNRAS, 484, 3393, doi: [10.1093/mnras/stz233](https://doi.org/10.1093/mnras/stz233)
- Zwaan, M. A., Liske, J., Péroux, C., et al. 2015, MNRAS, 453, 1268, doi: [10.1093/mnras/stv1717](https://doi.org/10.1093/mnras/stv1717)